Title: Enantiomeric excess dependent splitting of NMR signal through co-ligand dynamic exchange in a coordination complex

Authors

Kazuyoshi Takimoto,[1,2] Shinsuke Ishihara,[2*] Jan Labuta,[2*] Václav Březina,[3] Daniel T. Payne,[4] Jonathan P. Hill,[2] Katsuhiko Ariga,[2,5] Masato Sumita,[2,6] Shigeki Mori[7] and Hisako Sato[1]

Affiliations

[1]Department of Chemistry, Graduate School of Science and Engineering, Ehime University, Matsuyama, Ehime 790-8577, Japan

[2]International Center for Materials Nanoarchitectonics (WPI-MANA), National Institute for Materials Science (NIMS), 1-1 Namiki, Tsukuba, Ibaraki 305-0044, Japan

[3]Department of Macromolecular Physics, Faculty of Mathematics and Physics, Charles University, V Holešovičkách 2, 180 00 Prague 8, Czech Republic

[4]International Center for Young Scientists (ICYS), National Institute for Materials Science (NIMS), 1-1 Namiki, Tsukuba, Ibaraki 305-0044, Japan

[5]Department of Advanced Materials Science, Graduate School of Frontier Sciences, The University of Tokyo, Kashiwa, Chiba 277-8561, Japan

[6]Center for Advanced Intelligence Project, RIKEN, 1-4-1 Nihombashi, Chuo-ku, Tokyo 103-0027, Japan

[7]Advanced Research Support Center, Ehime University, Matsuyama, Ehime 790-8577, Japan

*Corresponding authors

E-mail: ISHIHARA.Shinsuke@nims.go.jp, LABUTA.Jan@nims.go.jp

Abstract

A coordination complex (**L**·2Zn·3**C**), where **L** is a prochiral ligand and **C** is an exchangeable acetate co-ligand, exhibits symmetrical splitting of ^{1}H-NMR resonances due to **L**, which is proportional to the enantiomeric excess (*ee*) of a chiral guest co-ligand, 2-phenoxypropionic acid (**PPA**). The NMR resonances remain split even in dilute solution due to the high stability of complex with chiral guest.

Main text:

Enantiomers of a chiral substance have non-superimposable structures, but exhibit identical nuclear magnetic resonance (NMR) spectra.[1] Thus, it is not possible to determine the enantiomeric excess (*ee*) of a chiral substance from NMR spectra of simple mixtures of enantiomers. However, it was recently discovered that the addition of a symmetrical prochiral host molecule to solutions containing chiral analytes can be used to estimate *ee* through a mechanism involving rapid exchange of hydrogen-bonded analyte-host complexes.[2] In those systems, NMR resonances of the prochiral host molecules show *ee* dependent splitting due to an averaging of chemical shift non-equivalency induced by the chiral analyte.[2] For this to occur, host symmetry requirements and guest binding strength are critical parameters in the intermolecular information transfer process, and eventually allow chiral information to be retrieved from the NMR spectrum of the prochiral host. This phenomenon does not depend on the formation of diastereomers since 1:1 analyte-host complexes (maintaining enantiomeric relationship) also exhibit *ee*-dependent splitting of NMR peaks.[2d,2f] Although intermolecular transfer of chemical shift non-equivalency is generally weak when observed in solution-state NMR spectra,[3,4] well resolved peak splitting (around 0.1 ppm) of NMR signals of enantiotopic protons in prochiral hosts can be observed under appropriate conditions.[2] This phenomenon offers NMR *ee* sensing based on prochiral molecules, so-called prochiral solvating agents (*pro*-CSAs).[2a] Methods based on *pro*-CSAs are distinct from conventional NMR chiral sensing methods,[1,5] which utilize chiral auxiliaries for derivatization of enantiomers as diastereomers, or chiral solvating agents. The operation of *pro*-CSAs is unique in that neither *pro*-CSA nor NMR involve chiral factors, so that the technique is neutral with respect to chirality.[6] However, all *pro*-CSAs so far reported employ hydrogen-bonds for binding of chiral guests, which might limit applicability of *pro*-CSAs under different conditions (e.g., at low concentration or where hydrogen bonds might not be sufficiently strong).

In comparison to hydrogen bonds, coordinate bonds are usually stronger,[7] and coordination complexes containing chiral ligands are widely used as chiral-solvating agents.[1,5a–5c] Thus, the incorporation of coordination bonds seems to be a promising means for broadening the applicability of the *pro*-CSA concept. However, operation of *pro*-CSA methods requires fast exchange of chiral guests at the prochiral host's binding site for averaging of chemical shift non-equivalency.[2a,2g] In general, strong guest binding leads to slow exchange,[2g,8] so that it was not clear whether or not coordination bonds could be incorporated in *pro*-CSA sensing systems.

Herein, we report the first example of *pro*-CSA activity based on guest exchange involving coordination bonds. Salen-like ligand **L** was designed to incorporate a prochiral benzylic CH$_2$ reporting group in the vicinity of a transition metal coordination complex (here Zn^{2+}) and an exchangeable co-ligand (**C**) (either acetate (AcO) or chiral guest, 2-phenoxypropionic acid (**PPA**)). Salens[9] are tetradentate ligand molecules prepared from ethylene diamine and salicylaldehydes. Simple salens possess C_2-symmetry. However, since only four symmetry space groups (C_s, C_{2v}, D_{2d}, S_4) lead to splitting of prochiral NMR signals in a chiral field (e.g., in a chiral liquid crystal),[3] we have replaced one of the salicyl arms of salen with a benzylic group thus breaking overall symmetry to C_s (Fig. 1a).

The prochiral benzylic CH_2 in **L** was expected to act as a chirality (i.e., *ee*) reporter group when chiral guests bind to the metal centre of **L·2Zn·3C** through co-ligand exchange. (Fig. 1a). Despite chirality of **L·2Zn·3C** in its crystal structure (that is, a static form in solid-state), concurrent fast exchange of its chirality and co-ligands in solution state renders **L·2Zn·3C** the primary example of *pro*-CSA based on a coordination complex. In fact, the ^{1}H-NMR resonance due to the benzylic CH_2 in the ternary mixture (**L** + Zn(AcO)$_2$ + **PPA**) exhibits *ee*-dependent splitting (Fig. 1b). Binary mixtures of **L** and **PPA** exhibit no splitting of NMR signals, indicating that Zn^{2+} plays an indispensable role. It is notable that *ee*-dependent NMR splitting in the coordination complex occurs even in dilute solution due to the lack of chiral guest dissociation in the co-ligand exchange system. This is in contrast to a previously reported hydrogen-bonded host-guest system.[2] This work provides the primary evidence for *pro*-CSA activity in coordination complexes, gives new insights into chiral transfer events in metal-ligand complexes, and suggests a substantial new subject of investigation for chiral processes involving dynamic coordination bonding.
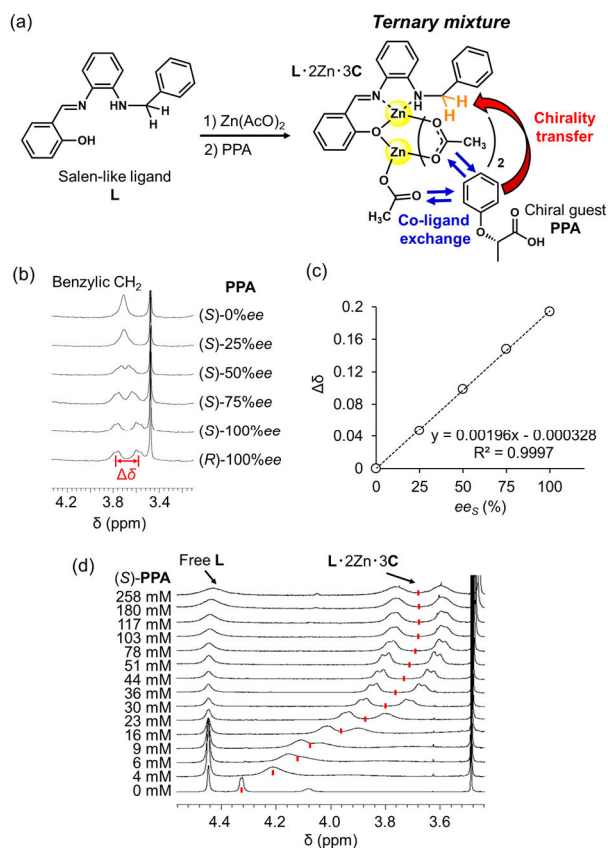

Fig. 1 (a) Chirality transfer based on a ternary mixture containing **L**, Zn(AcO)$_2$ and **PPA**. (b) ^{1}H-NMR spectra (in CDCl$_3$, 25 °C) of **L·2Zn·3C** (benzylic CH_2 resonance) in the presence of **PPA** (80 mM) with various *ee*, [**L**]$_{total}$ = 10 mM. (c) Dependency of magnitude of splitting ($\Delta\delta$) on *ee* of **PPA** (as obtained from Fig. 1b). (d) NMR titration (in CDCl$_3$, 27 °C) of **L·2Zn·3C** with (*S*)-**PPA** (0−258 mM), [**L**]$_{total}$ = 10 mM.

Salen-like ligand **L** (see SI and Figs. S1−S4 for synthesis) was mixed with two equivalents of zinc(II) acetate dihydrate in dichloromethane/methanol (3/1 v/v). After removal of solvents, a Zn^{2+} complex of **L** containing two zinc cations and three acetates (**L·2Zn·3AcO**, stoichiometry will be discussed later) was obtained as a pale yellow solid (schematic structure is shown in Fig. 1a; for NMR characterisation see Figs. S5, S6). The use of diamagnetic Zn^{2+} as the metal cations for coordination prevents broadening and paramagnetic shifts in NMR spectra (see Fig. S7 for broad spectrum of Cu^{2+} complex).

In this study, 2-phenoxypropionic acid (**PPA**) was used as a chiral guest co-ligand due to possible strong induction of chemical shift non-equivalency and its excellent solubility in $CDCl_3$.[2f] As shown in Fig. 1b (for complete spectra see Fig. S8), the ^{1}H-NMR resonance due to the benzylic CH_2 group in **L·2Zn·3C** is symmetrically split depending on the *ee* of **PPA** at 25 ˚C (Fig. 1b), and also at higher temperatures (for data at 50 ˚C see Fig. S9). The magnitude of splitting ($\Delta\delta$), a measure of chemical shift non-equivalency, has a linear relationship with *ee* of **PPA** (Fig. 1c), which is one of the fundamental properties of *pro*-CSA activity.[2a] Reduction in the *ee* of **PPA** leads to corresponding reductions in the magnitude of splitting ($\Delta\delta$) with no splitting observed for (*rac*)-0% *ee* **PPA** due to complete averaging (or "cancellation") of chemical shift non-equivalency caused by fast exchange between (*R*)- and (*S*)-**PPA**. ^{1}H-NMR titration of **L·2Zn·3C** with **PPA** revealed that the resonance due to the benzylic CH_2 group gradually splits and shifts upon addition of (*S*)-**PPA** (0 − 258 mM) with saturation around 80 mM of **PPA** (Fig. 1d and Fig. S10 for complete spectra). The split NMR signals consist of a characteristic AB-type second order *J*-coupled doublet of doublets with "roofing" effect, indicating that the split signals originate from the geminal benzylic CH_2 group of the same molecule. The AB spectral pattern was carefully fitted in order to extract the $\Delta\delta$ values.[2d] Upfield NMR shifts in **L·2Zn·3C** in the presence of **PPA** can be ascribed to the shielding-effect of the phenyl ring in **PPA** since addition of acetic acid does not cause this shift (Fig. S14).

It should also be noted that ^{1}H-NMR spectra of a binary mixture containing **L** and (*S*)-**PPA** in $CDCl_3$ shows no splitting (Fig. S11) and the chemical shift of **L** hardly varies upon addition of (*S*)-**PPA**. These results indicate only weak or no interaction between **L** and **PPA** in the absence of $Zn(AcO)_2$ in turn indicating that the latter plays a key role in efficient transfer of chiral information.

Importantly, we found no concentration dependencies (10 and 100 times dilution) in NMR spectra of the ternary mixture **L·2Zn·3C** with 8 equiv. of **PPA** (Fig. 2a). Since co-ligands (AcO and **PPA**) are constantly present proximal to the complex as charge-balancing anions, dissociation of co-ligands (e.g., **L·2Zn·3C** ⇄ [**L·2Zn·2C**]$^+$ + [**C**]$^-$) is unlikely to occur even in dilute solutions. For comparison, we also tested a previously reported hydrogen-bond-type *pro*-CSA (benzylamine + (*S*)-**PPA**)[2f], confirming strong concentration dependence based on dissociation of the host-guest complex in dilute solution (Fig. 2b). Thus, the lack of concentration dependency for the existence of the complex is an important feature of the metal-ligand-complex-type *pro*-CSAs, and also enables operation of NMR *ee*-sensing involving small quantities of materials.
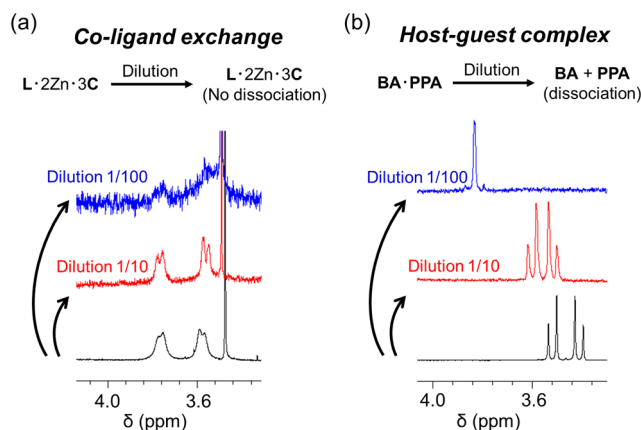
Fig. 2 (a) ^{1}H NMR spectra (benzylic CH$_2$) of a mixture of **L** (10 mM), Zn(AcO)$_2$ (20 mM) and (*S*)-**PPA** (80 mM) in CDCl$_3$ (25 ˚C) diluted with CDCl$_3$ by factors of 10 and 100. (b) ^{1}H NMR spectra (benzylic CH$_2$) of a mixture of benzyl amine (**BA**, 10 mM) and (*S*)-**PPA** (80 mM) in CDCl$_3$ (25 ˚C) diluted with CDCl$_3$ by factors of 10 and 100. See Figs. S12 and S13 for complete spectra.

Fig. 1d implies that **PPA** has higher priority than AcO as a co-ligand in **L**·2Zn·3**C** since addition of 80 mM **PPA** to a mixture of **L** (10 mM) and Zn(AcO)$_2$ (20 mM) leads to saturation of NMR spectral variations (note that AcO is contained at 40 mM). The observed large affinity of **PPA** could be due to the ether oxygen that can also participate in coordination at Zn^{2+}. As expected, replacement of **PPA** with AcO requires addition of a large excess of acetic acid (AcOH) into the mixture of **L**·2Zn·3AcO with 4 equiv. of **PPA** (see Fig. S15). The relative affinity K_{PPA}/K_{AcOH} of **PPA** over AcOH was estimated using a competitive binding model to be 12 (Fig. S28).

X-ray crystal structural analysis was performed on a single crystal of the **L**·2Zn·3AcO complex (Fig. 3). **L** binds two Zn^{2+} associated with three charge-compensating acetates. The acetate most remote from the benzyl group has two different C-O bond lengths (C25-O6 = 1.280 Å and C25-O7 = 1.241 Å), indicating localization of the carbonyl double bond (C=O) and single bond (C-O$^-$). On the other hand, the two bridging acetates have C-O bond lengths (approx. 1.25~1.26 Å) suggesting delocalization due to their bridging nature. In addition, chirality of the **L**·2Zn·3AcO complex was confirmed due to the presence of a chiral point at the benzylic nitrogen atom of **L** (Fig. S22a).

Stoichiometry in the crystal structure (**L**:Zn^{2+} = 1:2) is consistent with results from NMR and UV-Vis titrations (solution state) analysed by singular value decomposition (SVD) analysis (see Figs. S16, S23−S27).[10,11] During the NMR titration, ^{1}H-NMR signals due to free **L** gradually disappeared, and new ^{1}H NMR signals ascribed to the zinc complex emerged (Fig. S16). Thus, exchange between free and complexed **L** is slow on the NMR timescale.

CD spectra of the **L**·2Zn·3**C** complex in the presence of **PPA** showed *ee* dependent CD signals around 300−400 nm (see Fig. S22b) suggesting that chirality of **L**·2Zn·3**C** is switchable and slightly biased to one form by interaction with non-racemic **PPA**, which results in generally weak CD signals

5

(Fig. S22b). The two enantiomers of the **L·2Zn·3C** complex are most likely in fast exchange in solution (on the NMR timescale) due to fast disruption and reforming of coordination bonds. This hypothesis is supported by the appearance of single singlet resonances in ^{1}H-NMR and ^{13}C-NMR spectra originating from acetate CH_3 (if the exchange were slow, at least three singlets should be observed, Figs. S5, S6).
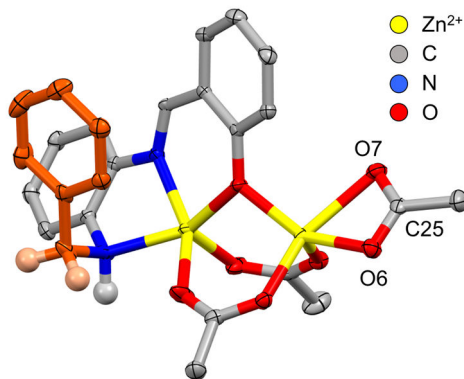

Fig. 3 X-ray crystal structure of zinc complex, **L·2Zn·3AcO**. Thermal ellipsoids are drawn at the 50% probability level, and H atoms are omitted for clarity (except for benzylic CH_2 and NH shown as small spheres with arbitrary radius). Benzyl group is highlighted in orange. CCDC deposit number: 1957329.

Since a single crystal could not be obtained from the ternary mixture (i.e., **L** + Zn(AcO)$_2$ + **PPA**), DFT calculations were performed to estimate the proximity of **PPA** to the reporting group (i.e., benzylic CH_2 in **L**) (Fig. 4). First, the zinc complex **L·2Zn·3AcO** (Fig. 3) was optimized to minimum energy (vacuum, 0 K), then each of the three acetates was substituted with (*S*)- or (*R*)-**PPA** (see Figs. S32 and S33 for details). The replacement of one acetate with (*S*)- or (*R*)-**PPA** yields six different diastereomers because of the chirality of the zinc complexes when they are in static form. The calculated energy differences between the six diastereomers are negligibly small suggesting that acetate substitution is not regioselective. **PPA** substitution of acetate-1 (Fig. 4), which is adjacent to the benzyl group of the complex, ought to yield the greatest chemical shift non-equivalency (originating from shielding effects of the phenyl group in **PPA**). In reality, in the presence of excess **PPA**, the zinc complex will bind multiple **PPA** concurrently (see ESI-MS result in Figs. S29−S31) leading to 16 possible diastereomeric species for **L·2Zn·3PPA**. However, it should be noted that formation of diastereomers is not the origin of *ee*-dependent NMR splitting in *pro*-CSAs,[2d,2f] and co-ligand exchange is fast on the NMR time scale. Although we provide plausible structures for triple **PPA** substitution modes (i.e., **L·2Zn·3PPA**) in Fig. S34, there will also be a large influence based on the arbitrary initial geometries used for DFT calculations.

There could also be other contributing interactions such as coordination of the ether oxygen of **PPA** to Zn^{2+} or intramolecular C-H···O hydrogen bonding interactions. This is supported by the lack of

induced splitting in NMR resonances of **L**·2Zn·3**C** in the presence of another chiral acid, (*S*)-2-(4-isobutylphenyl)propanoic acid (ibuprofen), which lacks similarly positioned ether oxygen atoms (Fig. S17). The reasons for these large differences in the chiral transfer processes in the metal-ligand complexes caused by only subtle changes in the molecular structure are now under investigation. Also, other chiral guests such as mandelic acid and 1-phenylethylamine did not induce NMR splitting (Figs. S18 and S19), and CDCl3 was the best solvent among four solvents tested (CDCl3, THF-d8, acetone-d6, and methanol-d4) (Figs. S20 and S21). However, we believe that some limitations observed in the present system could be overcome by improved design of the metal-ligand-complex. In fact, our previous reports have revealed that elaborately-designed *pro*-CSA reagents (hydrogen-bonded system) can be versatile and are available for various chiral guests (carboxylic acid, amine, alcohol, ketone, and ester).[2d]
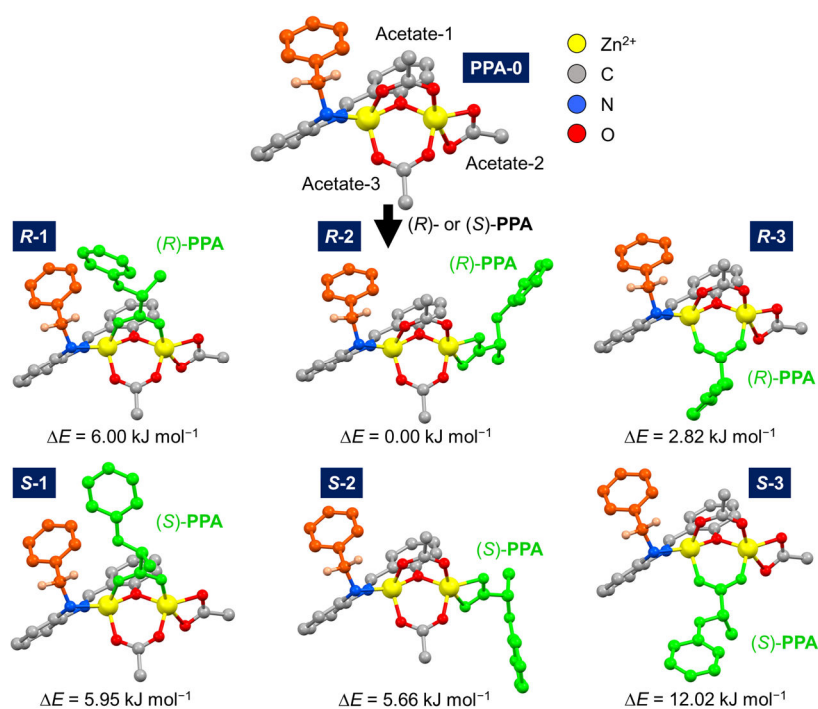

Fig. 4. X3LYP/6-31G(d) optimized structures and relative energies ΔE (kJ mol^{-1}) of **L**·2Zn·3**C** with each of the three acetates substituted by one **PPA** (in vacuum, 0 K). Benzyl groups (with two CH$_2$ protons) and **PPA** are highlighted in orange and green, respectively.

In conclusion, we have demonstrated a metal-ligand complex that exhibits *pro*-CSA activity. Prochiral ligand **L** reacts with Zn(AcO)$_2$ forming the dinuclear acetate-bridged complex **L**·2Zn·3AcO, whose co-ligand acetates are subject to dynamic exchange with chiral guest molecules (**PPA**), thus

establishing a ternary system with efficient intra-complex transfer of chiral information under a fast exchange regime. In contrast to a previously reported hydrogen-bonded system, *ee*-dependent NMR peak splitting in the coordination complex is possible even in dilute solutions due to a lack of chiral guest dissociation. We expect that this work not only provides a guide to design various types of *pro*-CSAs but also gives new insights into chiral transfer events in metal-ligand complexes.

Notes

The authors declare no competing financial interests.

References

1   (a) Parker, D. NMR determination of enantiomeric purity. *Chem. Rev.* **1991**, *91*, 1441−1457.; (b) Wenzel, T. J. *Discrimination of Chiral Compounds using NMR Spectroscopy*; John Wiley & Sons, 2007.

2   (a) Labuta, J.; Hill, J. P.; Ishihara, S.; Hanyková, L.; Ariga, K. Chiral Sensing by Nonchiral Tetrapyrroles. *Acc. Chem. Res.* **2015**, *48*, 521−529.; (b) Shundo, A.; Labuta, J.; Hill, J. P.; Ishihara, S.; Ariga, K. Nuclear Magnetic Resonance Signaling of Molecular Chiral Information Using an Achiral Reagent. *J. Am. Chem. Soc.* **2009**, *131*, 9494−9495.; (c) Labuta, J.; Ishihara, S.: Shundo, A.; Arai, S.; Takeoka, S.; Ariga, K.; Hill, J. P. Chirality Sensing by Nonchiral Porphines. *Chem. Eur. J.* **2011**, *17*, 3558−3561.; (d) Labuta, J.; Ishihara, S.; Šikorský, T.; Futera, Z.; A. Shundo, Hanyková, L.; Burda, J. V.; Ariga, K.; Hill, J. P. NMR spectroscopic detection of chirality and enantiopurity in referenced systems without formation of diastereomers. *Nat. Commun.* **2013**, *4*, 2188−2195.; (e) Labuta, J.; Ishihara, S.; Ariga, K.; Hill, J. P. Dynamic Processes in Prochiral Solvating Agents (pro-CSAs) Studied by NMR Spectroscopy. *Symmetry* **2014**, *6*, 345−367.; (f) Ishihara, S.; Labuta, J.; Futera, Z.; Mori, S.; Sato, H.; Ariga, K.; Hill, J. P. NMR Spectroscopic Determination of Enantiomeric Excess Using Small Prochiral Molecules. *J. Phys. Chem. B* **2018**, *122*, 5114−5120.; (g) Labuta, J.; Ishihara, S.; Hill, J. P. *meso*-Tetraphenylporphine as a prochiral solvating agent (pro-CSA): A physicochemical study. *J. Porphyrins Phthalocyanines* **2020**, *24*, 320−329.; (h) Labuta, J.; Futera, Z.; Ishihara, S.; Kouřilová, H.; Tateyama, Y.; Ariga, K.; Hill, J. P. Chiral Guest Binding as a Probe of Macrocycle Dynamics and Tautomerism in a Conjugated Tetrapyrrole. *J. Am. Chem. Soc.* **2014**, *136*, 2112−2118.

3   Lesot, P.; Aroulanda, C.; Zimmermann, H.; Luz, Z. Enantiotopic discrimination in the NMR spectrum of prochiral solutes in chiral liquid crystals. *Chem. Soc. Rev.* **2015**, *44*, 2330−2375.

4 There are a few reports of splitting of NMR resonances in solution, however, their *ee* dependencies were not investigated. See (a) Fraser, R. R.; Petit, M. A.; Miskow, M. Separation of nuclear magnetic resonance signals of internally enantiotropic protons using a chiral shift reagent. Deuterium isotope effect on geminal proton-proton coupling constants. *J. Am. Chem. Soc.* **1972**, *94*, 3253−3254.; (b) Bilz, A.; Stork, T.; Helmchen, G. New chiral solvating agents for carboxylic acids: discrimination of enantiotopic nuclei and binding properties. *Tetrahedron Asymmetry* **1997**, *8*, 3999−4002.

5 (a) Zhao, Y.; Swager, T. M. Simultaneous Chirality Sensing of Multiple Amines by ^{19}F NMR. *J. Am. Chem. Soc.* **2015**, *137*, 3221−3224.; (b) Wang, W.; Xia, X.; Bian, G.; Song, L. A chiral sensor for recognition of varied amines based on ^{19}F NMR signals of newly designed rhodium complexes. *Chem. Comm.* **2019**, *55*, 6098−6101.; (c) Li, L. P.; Peng, H. L.; Ye, B. H. Chiral sensor for enantiomeric purity of amines, amino alcohols and amino esters based on bis-cyclometalated Ir(III) complex using ^{1}H NMR spectroscopy. *Inorg. Chim. Acta* **2018**, *482*, 691−697.; (d) Chen, Z.; Fan, H.; Yang, Shiwei; Bian, G.; Song, L. Chiral sensors for determining the absolute configurations of α-amino acid derivatives. *Org. Biomol. Chem.* **2018**, *16*, 8311−8317.; (e) Li, Y.; Yang, G.; He, C. Q.; Li, X.; Houk, K. N.; Cheng, J. Chirality Sensing of α-Hydroxyphosphonates by N-tert-Butyl Sulfinyl Squaramide. *Org. Lett.* **2017**, *19*, 4191−4194.

6 Alternatively, chirality discrimination (i.e., which is the major enantiomer in a sample) requires addition of a small amount of one of the known enantiomers (see refs. 2a and 2c).

7 Lawrance, G. A. *Introduction to Coordination Chemistry*; John Wiley & Sons Ltd., 2009.

8 Burgess, J. *Inorganic Reaction Mechanism*; The Chemical Society Burlington House: London, 1971, Vol. 2; Sykes, A. G.; *Kinetics of Inorganic Reactions*; Pergamon Press Ltd., 1966.

9 (a) Cozzi, P. G. Metal–Salen Schiff base complexes in catalysis: practical aspects. *Chem. Soc. Rev.* **2004**, *33*, 410−421.; (b) Katsuki, T. Catalytic asymmetric oxidations using optically active (salen)manganese(III) complexes as catalysts. *Coord. Chem. Rev.* **1995**, *140*, 189−214.; (c) Baleizão, C.; Garcia, H. Chiral Salen Complexes: An Overview to Recoverable and Reusable Homogeneous and Heterogeneous Catalysts. *Chem. Rev.* **2006**, *106*, 3987−4043.; (d) Burlov, A. S.; Koshchienko, Y. V.; Lyssenko, K. A.; Vasilchenko, I. S.; Alexeev, Y. E.; Borodkina, I. G.; Antipin, M. Y.; Garnovskii, A. D. Self-assembling tetranuclear complexes of a tridentate Schiff base. *J. Coord. Chem.* **2008**, *61*, 85−91.; (e) Belmonte, M. M.; Wezenberg, S. J.; Haak, R. M.; Anselmo, D.; Escudero-Ad´, E. C.; Benet-Buchholza J.; Kleij, A. W. Self-assembly of Zn(salphen) complexes: Steric regulation, stability studies and crystallographic analysis revealing an unexpected dimeric 3,3'-t-Bu-substituted Zn(salphen) complex. *Dalton Trans.* **2010**, *39*, 4541−4550.

10 Titration studies were performed in chloroform/methanol mixture since zinc acetate is insoluble in chloroform.

11 (a) Henry, E. R.; Hofrichter, J. *Methods in Enzymology*; Academic Press: 1992, 210, pp. 29–192; (b) Malinowski, E. R. *Factor Analysis in Chemistry*; Wiley-Interscience: USA, New York, 2002, pp. 1–432; (c) Březina, V.; Ishihara, S.; Lang, J.; Hanyková, L.; Ariga, K.; Hill, J. P.; Labuta, J. Structural Modulation of Chromic Response: Effects of Binding‐Site Blocking in a Conjugated Calix[4]pyrrole

Chromophore. *ChemistryOpen* **2018**, *7*, 323–335.; (d) Chahal, M. K.; Labuta, J.; Březina, V.; Karr, P. A.; Payne, D. T.; Ariga, K.; D'Souza, F.; Hill, J. P. Knock-on synthesis of tritopic calix[4]pyrrole host for enhanced anion interactions. *Dalton Trans.* **2019**, *48*, 15583–15596.; (e) Payne, D. T.; Chahal, M. K.; Březina, V.; Webre, W. A.; Ariga, K.; D'Souza, F.; Labuta, J.; Hill, J. P. Diporphyrin tweezer for multichannel spectroscopic analysis of enantiomeric excess. *Front. Chem. Sci. Eng.* **2020**, *14*, 28–40.; (f) Hanuš, J.; Chmelová, K.; Štěpánek, J.; Turpin, P.-Y.; Bok, J.; Rosenberg, I.; Točík, Z. Raman spectroscopic study of triplex-like complexes of polyuridylic acid with the isopolar, non-isosteric phosphonate analogues of diadenosine monophosphate. *J. Raman Spectrosc.* **1999**, *30*, 667–676.

Supporting Information

Enantiomeric excess dependent splitting of NMR signal through co-ligand dynamic exchange in a coordination complex

Kazuyoshi Takimoto, Shinsuke Ishihara,* Jan Labuta,* Václav Březina, Daniel T. Payne, Jonathan P. Hill, Katsuhiko Ariga, Masato Sumita, Shigeki Mori and Hisako Sato

*Corresponding authors: ISHIHARA.Shinsuke@nims.go.jp, LABUTA.Jan@nims.go.jp

Table of contents

1. Materials

Chemical reagents were purchased from Tokyo Chemical Industry (TCI), Wako Pure Chemical Industries, or Sigma-Aldrich Chemical Co. Ltd, and used without purification. NMR grade solvents, $CDCl_3$ (TCI), CD_3OD (Merck), tetrahydrofuran (THF)-d_8 (Kanto Chemical), and acetone-d_6 (Euriso-Top), were used as received. (*R*)-2-phenoxypropionic acid and (*S*)-2-phenoxypropionic acid (Wako Pure Chemical Industries, with guarantee of >98.0% *ee*) were used as received and treated as being optically-pure (i.e., 100% *ee*) for simplicity (see Fig. S35 for analysis of actual *ee*% by using chiral HPLC). (*R*)-2-phenoxypropionic acid and (*S*)-2-phenoxypropionic acid were mixed and ground in a mortar to prepare samples of 2-phenoxypropionic acid with known *ee*.

2. Methods

2.1 General methods

Unless noted otherwise, ^{1}H-NMR spectra were obtained using an AL300 BX spectrometer (JEOL, 300 MHz). In some cases, ^{1}H-NMR spectra were obtained using an AVIII500 (Bruker, 500 MHz) spectrometer. ^{13}C-NMR spectra were obtained using an AVIII500 (Bruker, 126 MHz) spectrometer. High resolution mass spectra (HRMS) were measured in fast atom bombardment (FAB) mode using a JMS-400V (JEOL) instrument. UV-visible (UV-Vis) electronic absorption spectra were recorded by using a UV-Vis spectrophotometer (SHIMADZU, UV-3600). Solutions were placed in a quartz cell with 1 cm optical length. Circular dichroism spectra were measured using a circular dichroism spectropolarimeter (JASCO, J-820). High resolution electrospray ionization mass spectrometry (ESI-MS) was performed using a Thermo Scientific Q-Exactive Plus with samples dissolved in $CDCl_3$.

2.2 X-ray crystallography

X-Ray diffraction analysis was performed using a Rigaku VariMax with a Saturn diffractometer using multilayer mirror monochromated Mo Kα radiation ($\lambda = 0.71073$ Å) at 100 ± 1 K. The crystals were mounted in cryoloops. Collection of the reflection intensities and determination of the cell parameters were performed using CrystalClear (Rigaku)[S1] and CrysAlisPro (Rigaku Oxford Diffraction).[S2] Data were corrected for Lorentz polarization and absorption effects. The structures were solved using SHELXT 2018/2[S3] and expanded using the Fourier technique. All calculations were performed using the CrystalStructure crystallographic software package[S4], and SHELXL-2018/3[S5] was used for structure refinement. Data were validated using PLATON.[S6]

2.3 Preparation of single crystals of zinc complex for X-ray crystal structure analysis

L dissolved in CH_2Cl_2 and zinc(II) acetate dihydrate dissolved in MeOH were mixed (**L**:zinc acetate = 1:2 molar ratio), and a crude crystalline product was obtained by evaporation of the solvents. The crude product was dissolved in CH_2Cl_2, and single crystals were grown by diffusion of hexane vapour.

2.4 Computational details

All calculations to estimate the total energies of the complexes were performed using the Gaussian 16 package (B.01).[S7] All geometries were optimized at the X3LYP/6-31G(d) level and their stabilities were confirmed through a vibrational analysis. We employed X3LYP/6-31G(d) to take non-bonding interactions (e.g., CH-π interaction) into consideration.[S8] Conformation dependence was checked by calculating other conformations of the complex. First, we tried two possible conformations of **PPA** in a test complex, and found that one conformation that involves two extra non-covalent interactions is more stable (Fig. S32). Then, the conformation of **PPA** was applied to other types of complexes shown in Fig. 4.

3. Syntheses

3.1 Synthesis of *N*-benzyl-1,2-phenylenediamine

1,2-Phenylenediamine dihydrochloride (3.00 g, 16.6 mmol) and potassium carbonate (4.60 g, 33.3 mmol) were mixed in a round bottom flask then vacuum dried and purged with dry nitrogen. Acetonitrile (100 mL) and benzyl bromide (1.97 mL, 16.6 mmol) were then added. The resulting suspension was stirred at 85 ºC for 20 hrs. After cooling to RT, acetonitrile was removed under reduced pressure. The residue was partitioned between CH_2Cl_2/brine, then the organic layer was separated and dried over anhydrous Na_2SO_4. After filtration, CH_2Cl_2 was removed under reduced pressure. The crude product was purified by column chromatography on silica gel (eluent: CH_2Cl_2), and obtained as a colorless oil (1.99 g, 10.2 mmol, Yield: 61%). ^{1}H-NMR (500 MHz, $CDCl_3$) in ppm: 7.24-7.40 (m, 5H, Ar-H), 6.67-6.82 (m, 4H, Ar-H), 4.31 (s, 2H, bzl-CH_2), 3.69 (s, 1H, NH), 3.33 (s, 2H, NH_2).
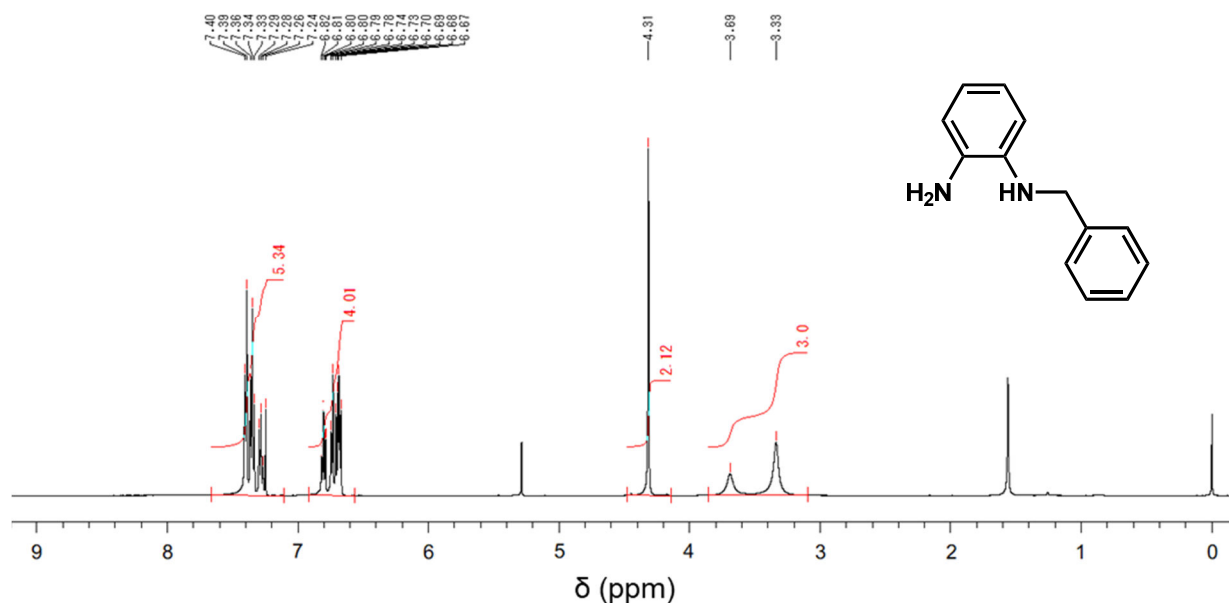

Figure S1. ^{1}H-NMR spectrum of *N*-benzyl-1,2-phenylenediamine measured in $CDCl_3$ (500 MHz, 27 ºC).

13

3.2 Synthesis of salen-like ligand (L)

Salen-like ligand (**L**) was synthesized by condensation of *N*-benzyl-1,2-phenylenediamine (64.9 mg, 0.33 mmol) with salicylaldehyde (0.034 mL, 0.32 mmol) in ethanol (superdehydrated, 20 mL). The solution was stirred at RT for 12 hrs, then solvent was removed under reduced pressure. The crude product was purified by column chromatography on silica gel (eluent: CH_2Cl_2/hexane = 1:1 (v/v)), and obtained as a yellow oil (78.6 mg, 0.26 mmol, Yield: 81%). ^{1}H-NMR (500 MHz, CDCl$_3$) in ppm: 12.90 (s, 1H, OH), 8.63 (s, 1H, N=CH), 6.66-7.42 (m, 13H, Ar-H), 4.84 (t, 1H, NH), 4.45 (d, 2H, bzl-CH$_2$). ^{13}C-NMR (126 MHz, CDCl$_3$) in ppm: 162.55, 160.83, 142.15, 139.33, 135.49, 133.26, 132.40, 129.47, 128.84, 128.50, 127.33, 127.21, 125.93, 119.79, 119.45, 118.23, 117.38, 117.27, 111.29, 48.01. HRMS/FAB$^+$(3-NBA) (m/z): calculated for $[C_{20}H_{18}N_2O+H]$ = 302.1419 m/z, found 302.1427 m/z.
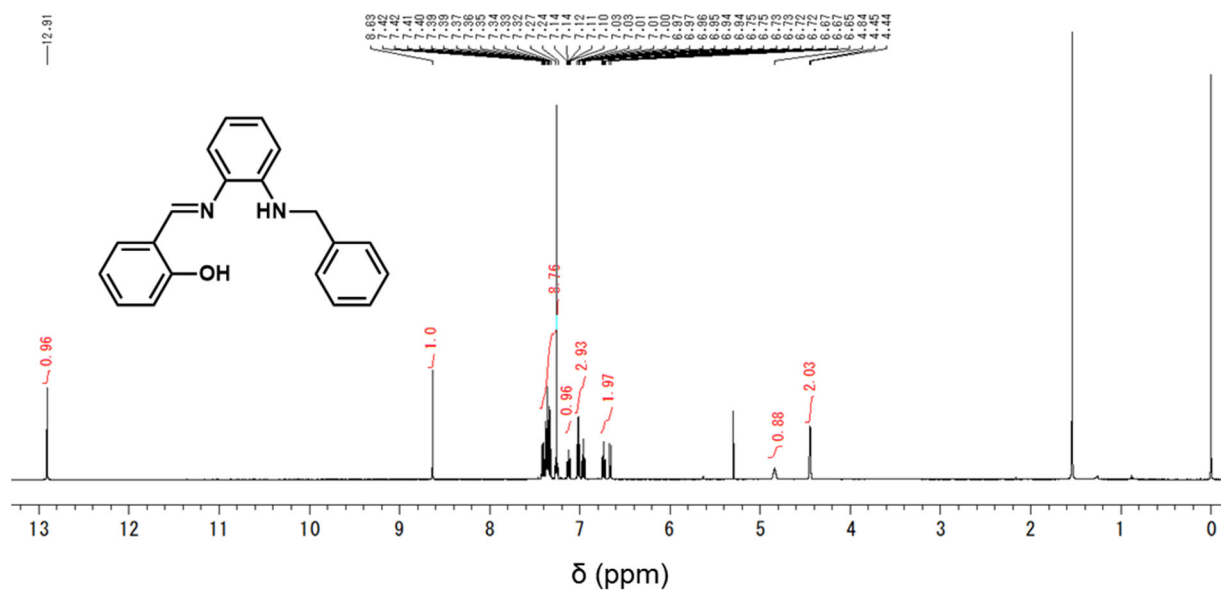

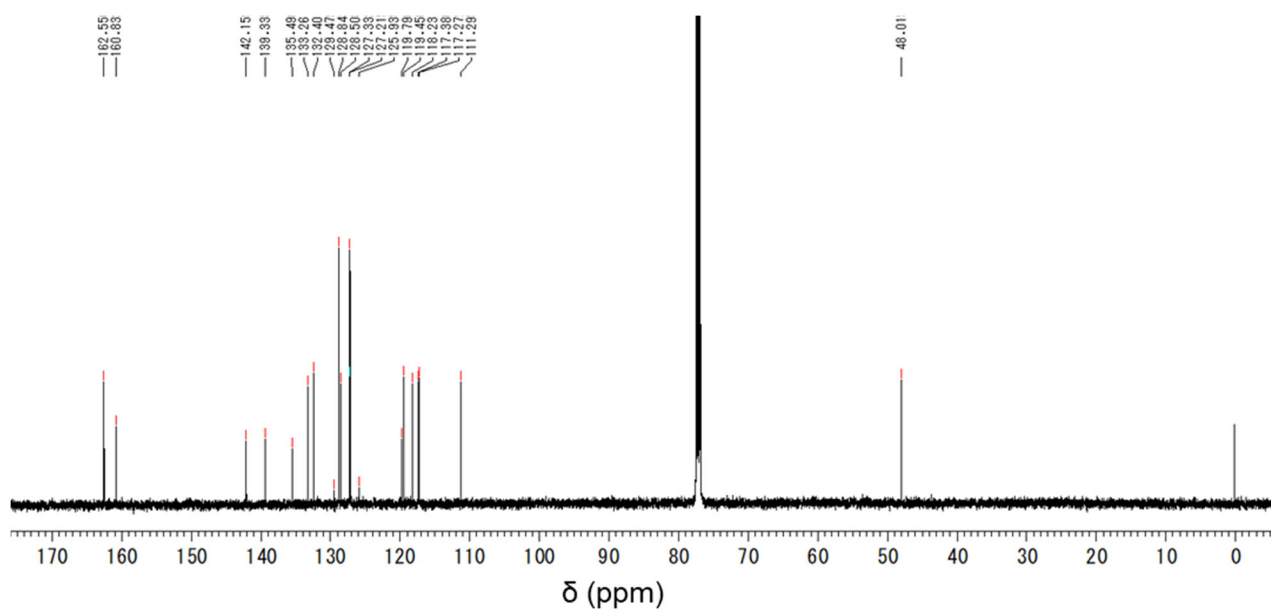**Figure S2.** ^{1}H-NMR spectrum of **L** in CDCl$_3$ (500 MHz, 27 °C).

14

Figure S3. ^{13}C-NMR spectrum of **L** in CDCl$_3$ (126 MHz, 27 ºC).

[Mass Spectrum]
Data : takimoto-20191003-001   Date : 03-Oct-2019 13:02
Instrument : MS700D
Sample : L
Note : Matrix:3NBA
Inlet : Direct   Ion Mode : FAB+
Spectrum Type : Normal Ion [EF-Linear]
RT : 5.78 min   Scan# : (30,37)   Temp : 3276.7 deg.C
BP : m/z 307.0954   Int. : 1602.85 (16807051)
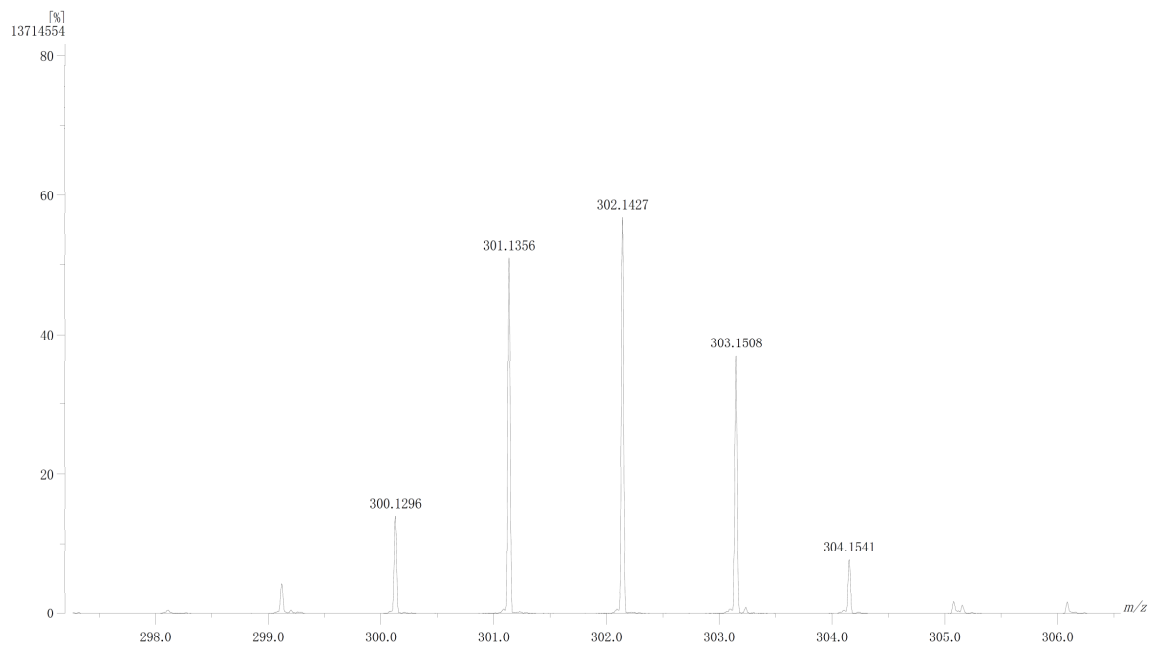Output m/z range : 297 to 307   Cut Level : 0.00 %

Figure S4. HRMS spectrum of **L** (FAB$^+$, 3-nitrobenzyl alcohol (3-NBA) as matrix).

15

3.3 Preparation of zinc complex

A solution of **L** (30.2 mg, 0.10 mmol) in CH_2Cl_2 (7.5 mL) was treated with two equivalents (in mole) of zinc(II) acetate dihydrate (44.0 mg, 0.20 mmol) in CH_3OH (2.5 mL). After removal of solvents, the mixture was dissolved in $CDCl_3$ to adjust concentration of $[L]_{total}$ as 10 mM. ^1H- and ^{13}C-NMR spectrum contained signals corresponding to free **L** and Zn^{2+} complex (see Fig. S5, S6), and NMR *ee* sensing was performed based on the observation of splitting of peaks in the spectrum of the Zn^{2+} complex.
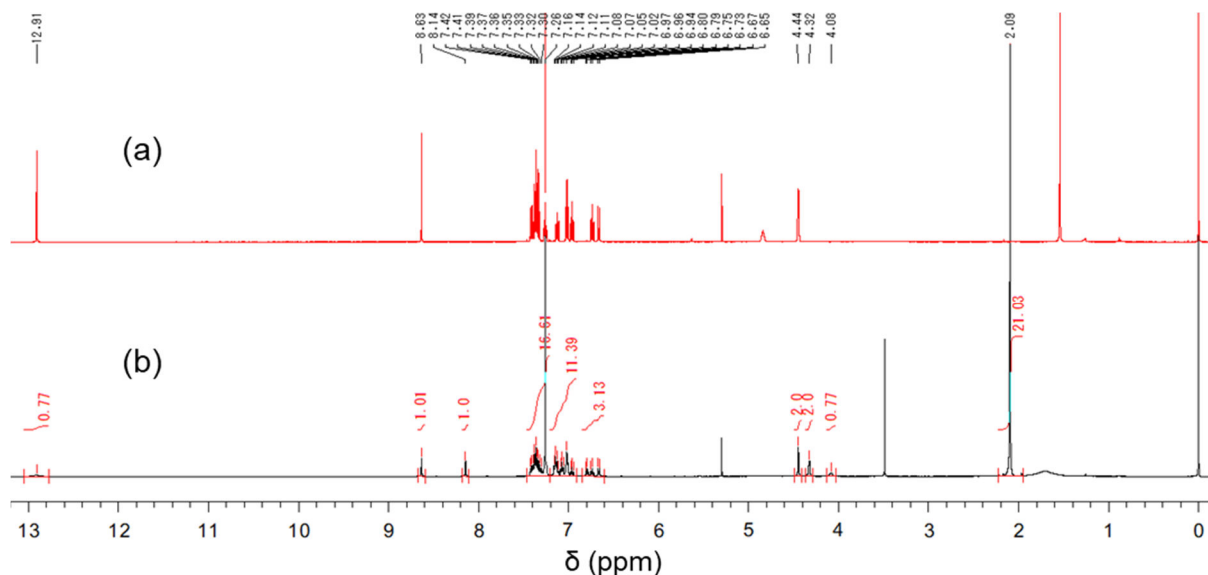

Figure S5. ^1H-NMR spectra of (a) **L** and (b) a mixture of **L** and zinc(II) acetate dihydrate in $CDCl_3$ (500 MHz, 27 ºC). Note that the peak due to acetate CH_3 at 2.03 ppm is a singlet.
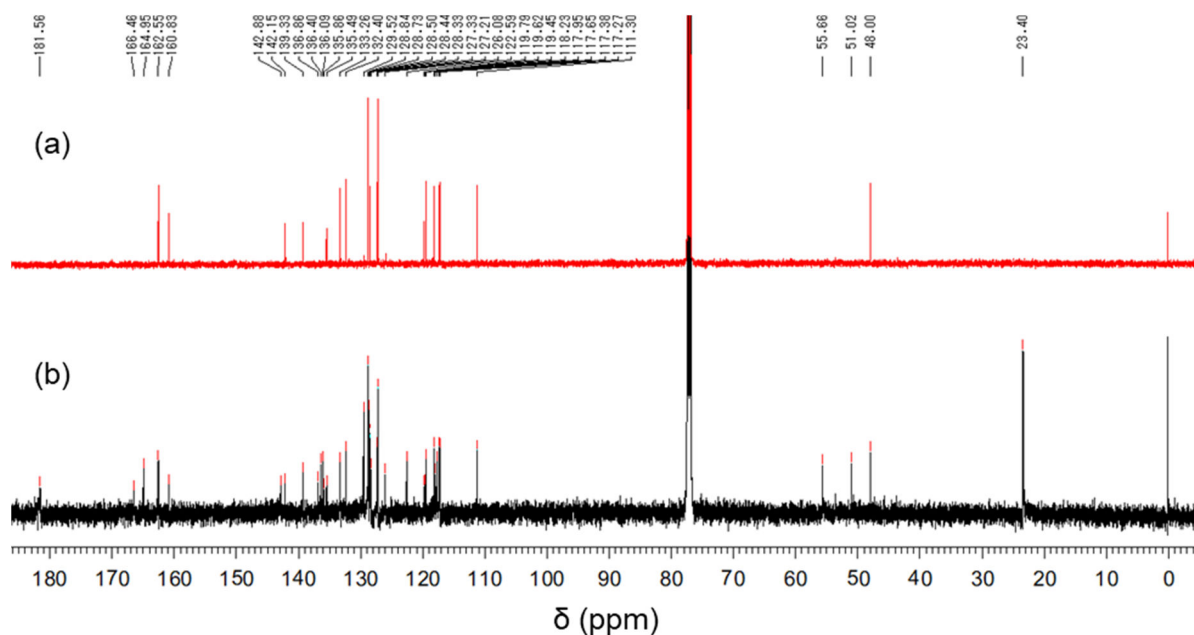

Figure S6. ^{13}C-NMR spectra of (a) **L** and (b) a mixture of **L** and zinc(II) acetate dihydrate in $CDCl_3$ (126 MHz, 27 ºC). Note that the peak due to acetate CH_3 at 23.4 ppm is a singlet.
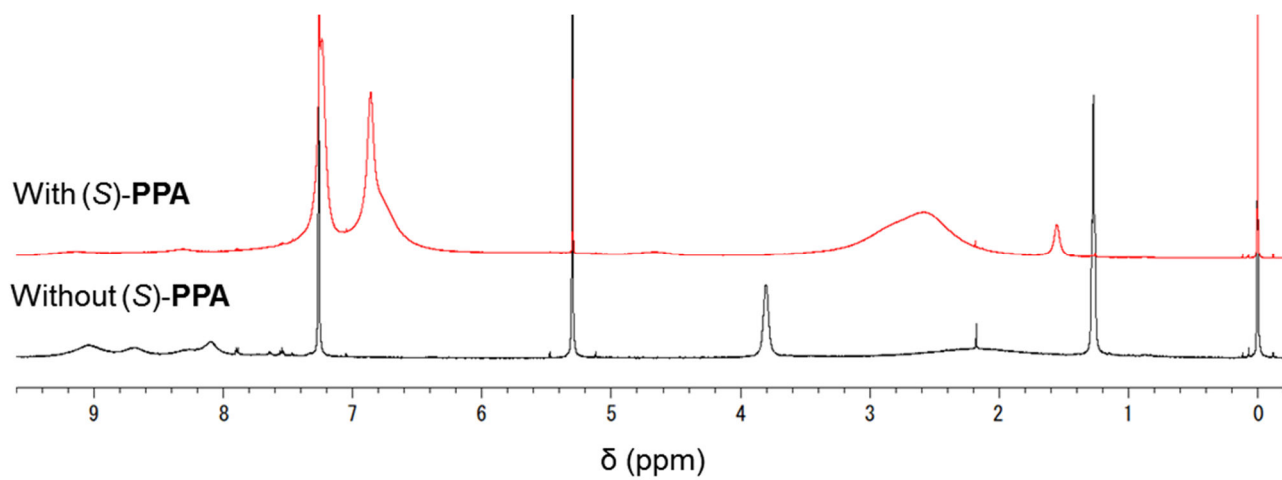
16

4. Additional NMR data

Figure S7. ^{1}H-NMR spectra (500 MHz) of a mixture of **L** (10 mM) and copper(II) acetate dihydrate (20 mM) in the presence and absence of (*S*)-**PPA** (80 mM) measured in CDCl$_3$ (25 ºC). NMR signals are broad due to paramagnetic effect of Cu^{2+}.
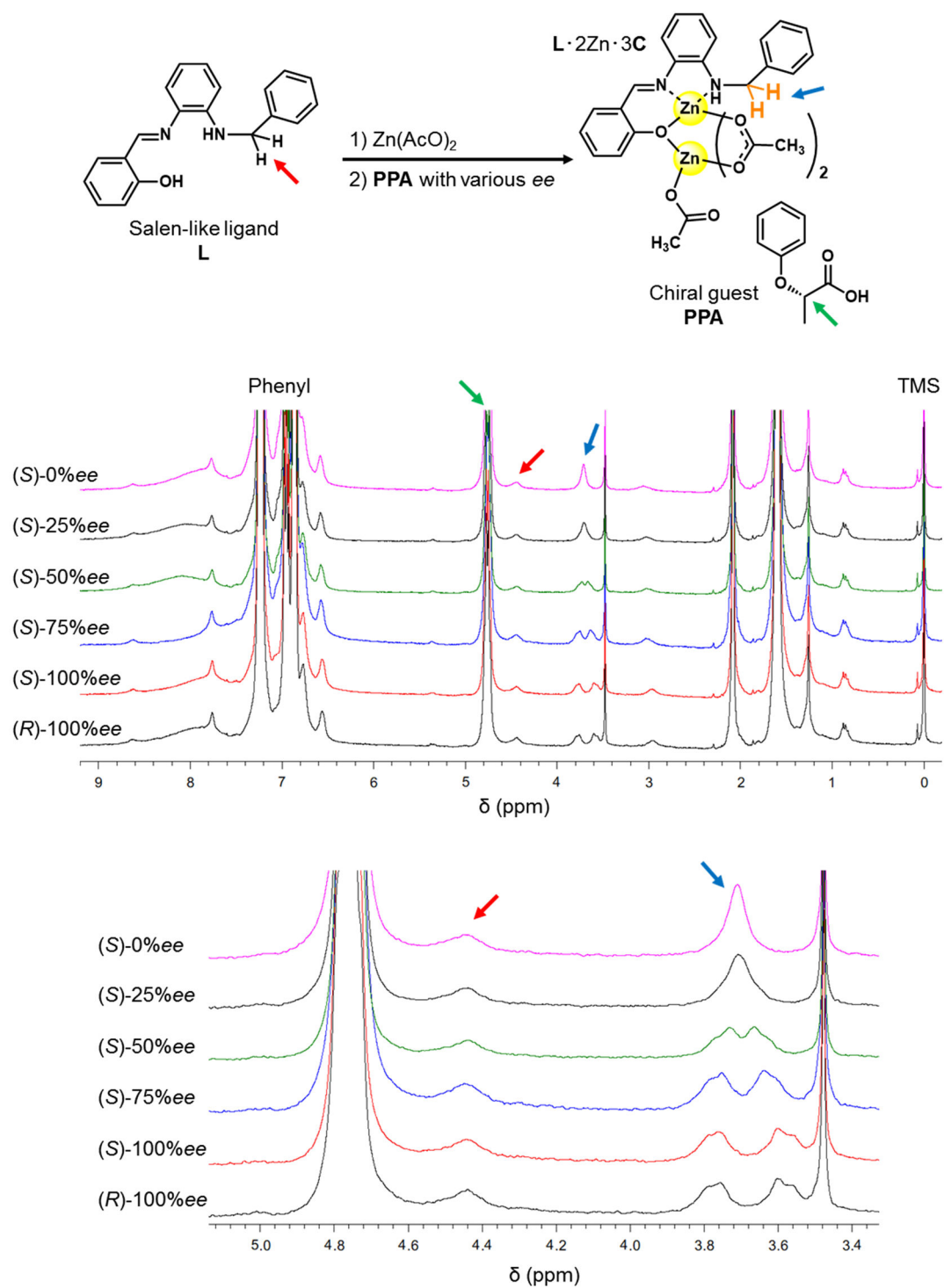
Figure S8. ^{1}H-NMR spectra (CDCl$_3$, 25 ºC) of **L·2Zn·3C** in the presence of **PPA** (80 mM) with various *ee*. [**L**]$_{total}$ = 10 mM
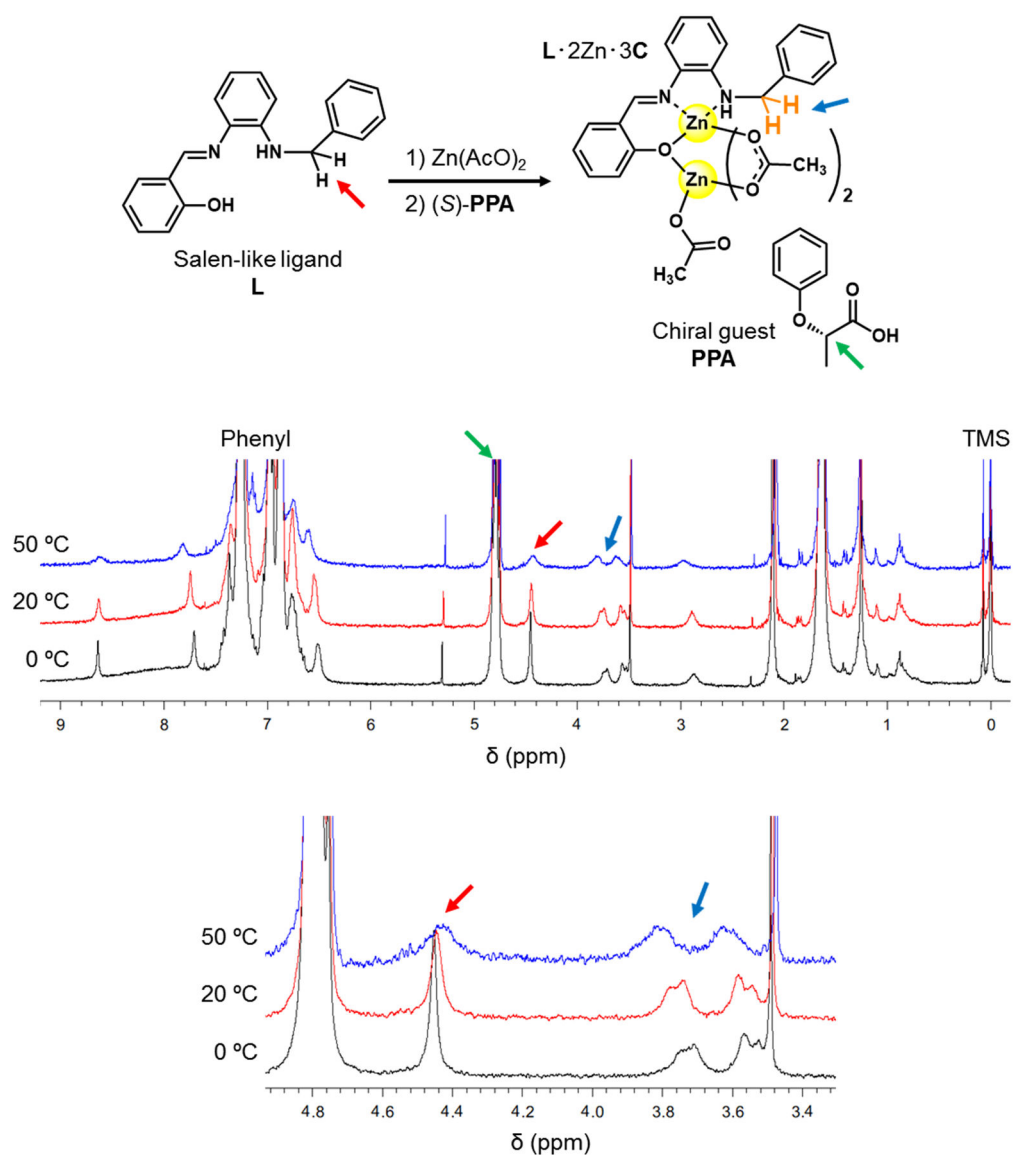
Figure S9. ^{1}H-NMR spectra of **L**·2Zn·3**C** in the presence of (*S*)-**PPA** (50 mM) measured in CDCl$_3$ at 0, 20, and 50 ºC. [**L**]$_{total}$ = 10 mM.

19
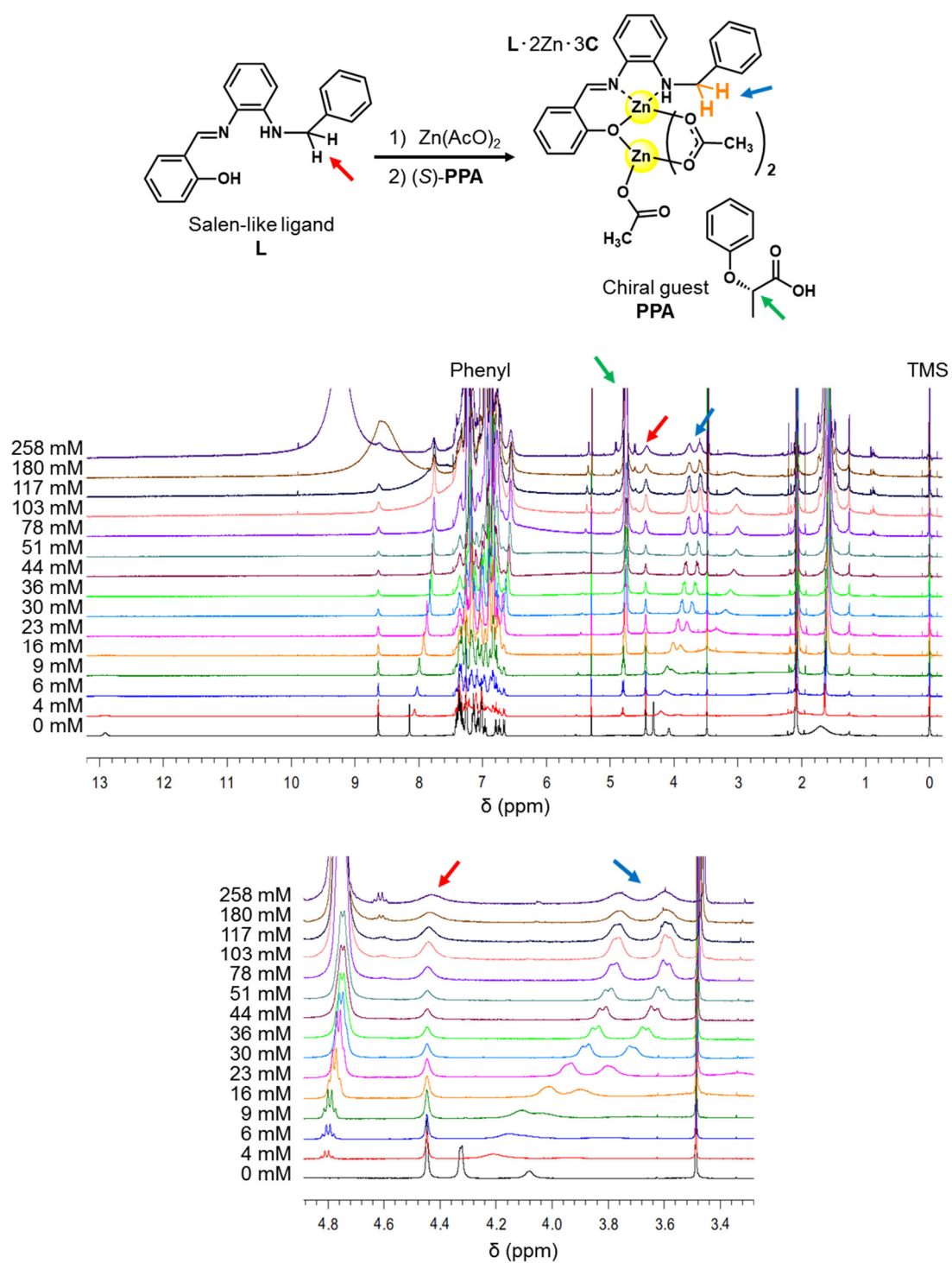
Figure S10. ^{1}H-NMR spectra (in CDCl$_3$, 27 ºC, 500 MHz) of **L·2Zn·3C** in the presence of (*S*)-**PPA** (0−258 mM). [**L**]$_{total}$ = 10 mM
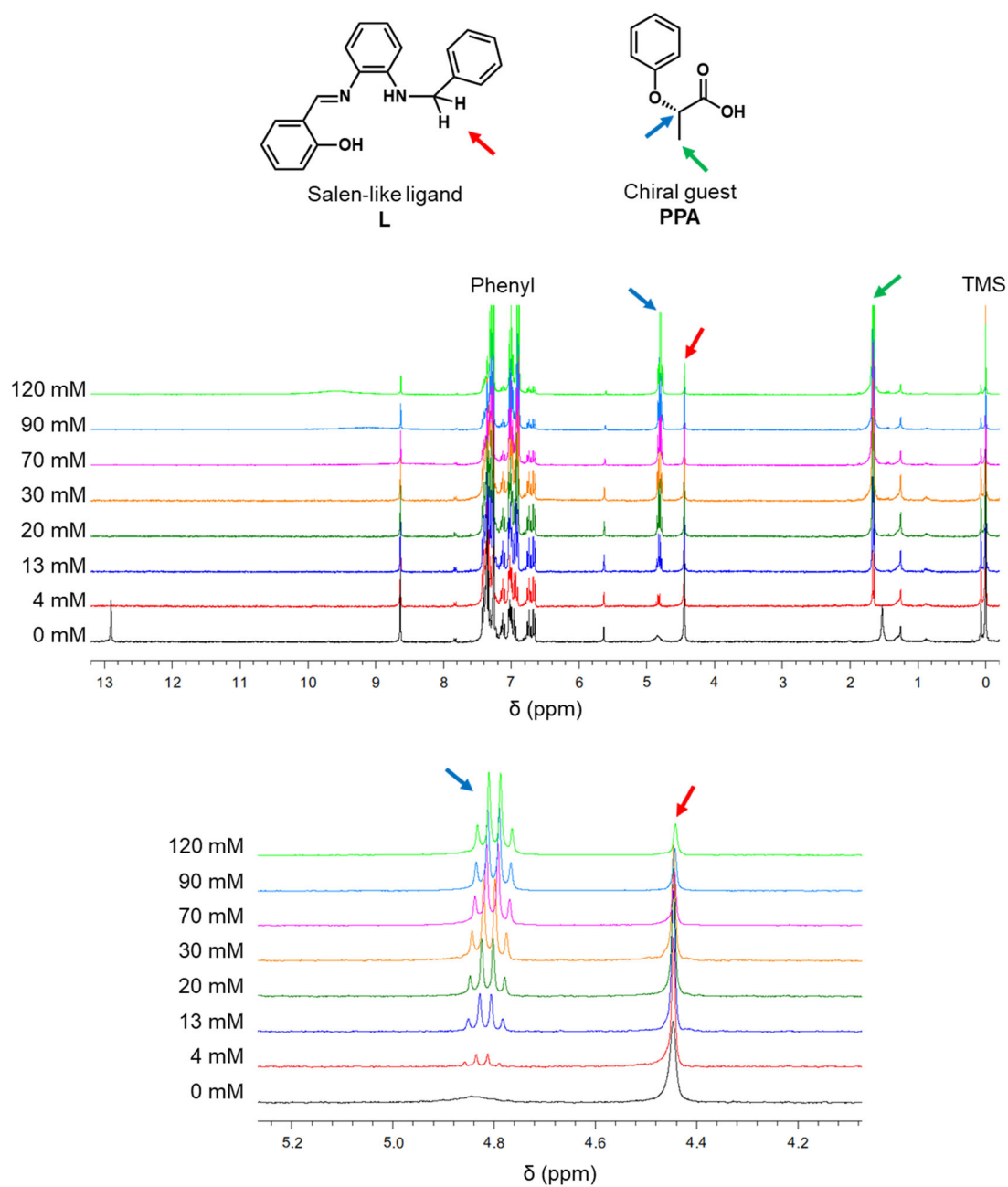
Figure S11. Comparison of the spectra of a binary mixture containing **L** and **PPA**. ^{1}H NMR spectra (in CDCl$_3$, 25°C) of **L** ([**L**]$_{total}$ = 10 mM) in the presence of (*S*)-**PPA** (0-120 mM). ^{1}H-NMR resonances due to **L** are influenced negligibly by (*S*)-**PPA**.
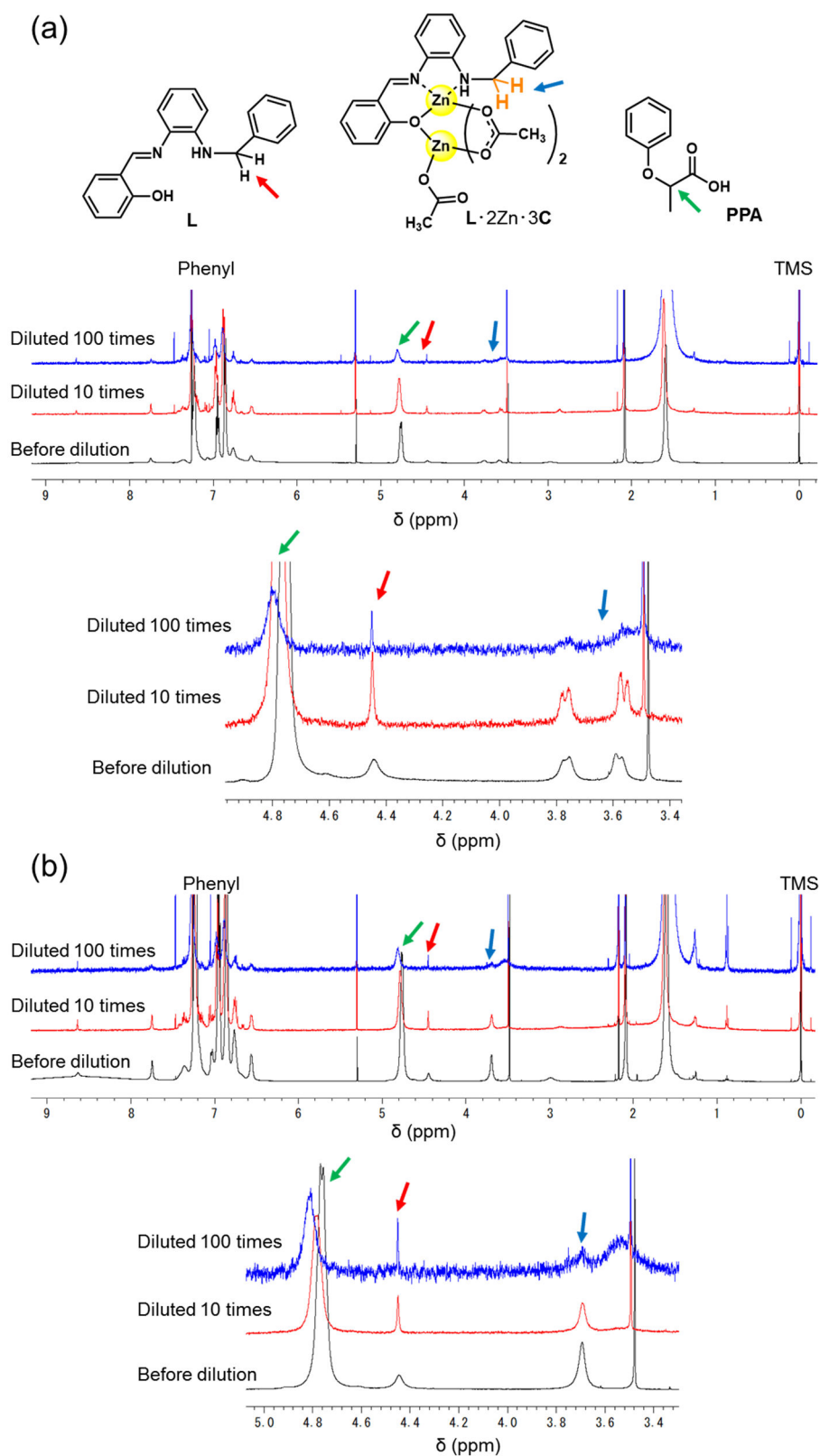
Figure S12. (a) ^{1}H NMR (500 MHz) spectra (benzylic CH$_2$) of a mixture of **L** (10 mM), zinc acetate (20 mM) and (*S*)-**PPA** (80 mM) in CDCl$_3$ (25 ºC) diluted with CDCl$_3$ by factors of 10 and 100. (b) ^{1}H NMR (500 MHz) spectra (benzylic CH$_2$) of a mixture of **L** (10 mM), zinc acetate (20 mM) and (*rac*)-**PPA** (80 mM) in CDCl$_3$ (25 ºC) diluted with CDCl$_3$ by factors of 10 and 100.
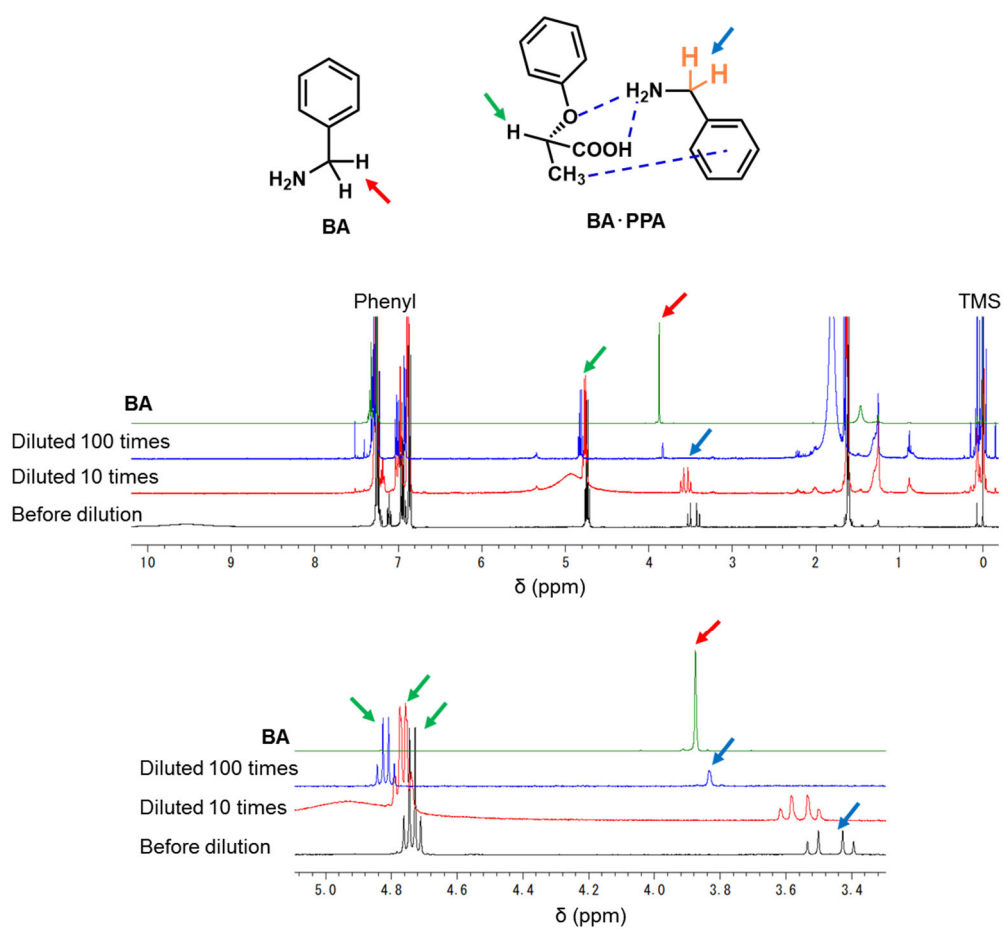
Figure S13. ^{1}H NMR spectra (benzylic CH$_2$) of a mixture of benzyl amine (**BA**, 10 mM) and (*S*)-**PPA** (80 mM) in CDCl$_3$ (25 ºC) diluted with CDCl$_3$ by factors of 10 and 100.

Titration of acetic acid (1). For comparison with the titration with (*S*)-**PPA** (Fig. 1d), we have performed titration of acetic acid with **L**·2Zn·3AcO (Fig. S14). NMR signal due to benzylic CH$_2$ in **L**·2Zn·3AcO does not shift upon addition of acetic acid due to co-ligand exchange of identical anions (**L**·2Zn·3AcO + AcOH ⇄ **L**·2Zn·3AcO + AcOH). We assign the upfield shift of benzylic CH$_2$ in **L**·2Zn·3AcO upon addition of **PPA** (Fig. 1d) as being due to ring-current (shielding) effects caused by the phenyl moiety in **PPA**.
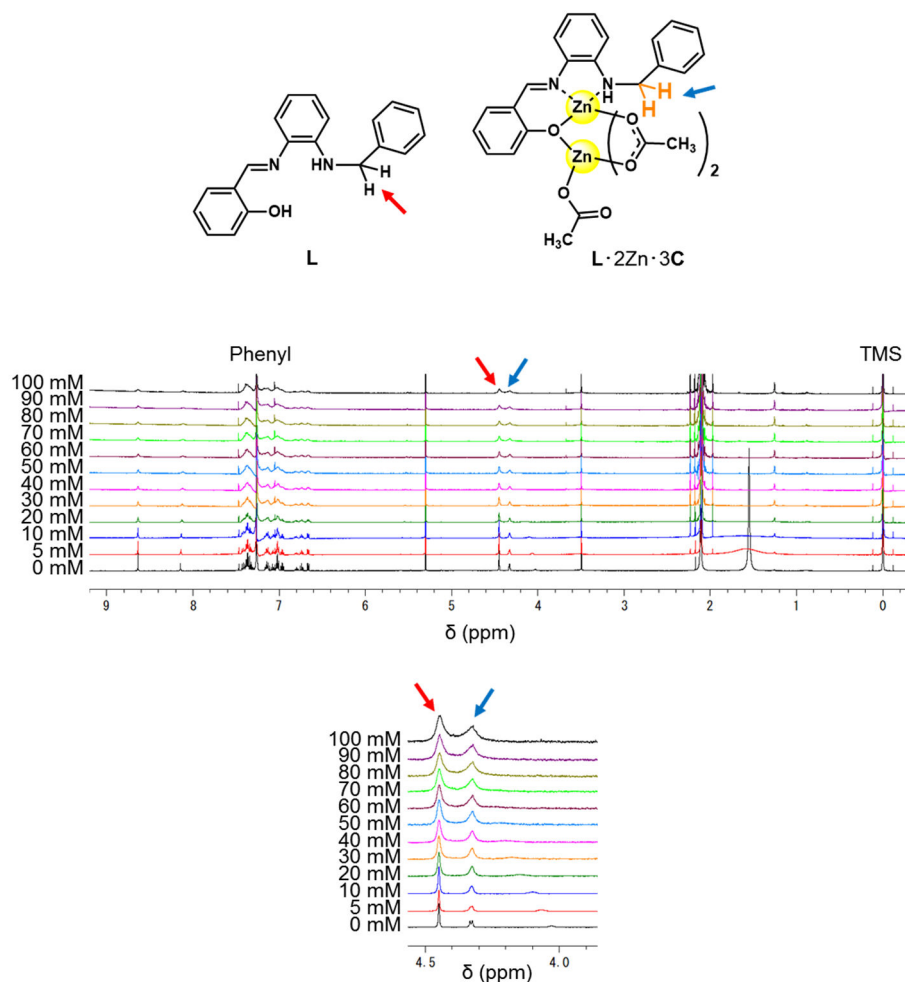

Figure S14. ^{1}H-NMR spectra (in CDCl$_3$, 25 ºC, 500 MHz) of **L**·2Zn·3AcO upon titration of acetic acid (0−100 mM). [**L**]$_{total}$ = 1 mM, [Zn^{2+}]$_{total}$ = 2 mM

Titration of acetic acid (2). We have also performed titration of acetic acid into a mixture of **L·2Zn·3AcO** and 4 equiv. of (*S*)-**PPA** (Fig. S15). A large excess of acetic acid was required to replace **PPA** with AcO (**L·2Zn·3PPA** + excess AcOH → **L·2Zn·3AcO** + **PPA**) indicating that the binding strength of **PPA** is much greater than AcO. This is reasonable based on the presence of ether oxygen in **PPA** that can participate in coordination to Zn^{2+} or other intramolecular interactions. In fact, in the titration of **PPA** into **L·2Zn·3AcO** (Fig. 1d), the replacement of AcO with **PPA** saturates at around 8 equiv. of **PPA** (in comparison to **L**) while the solution contains 4 equiv. of AcO. If the binding strengths of **PPA** and AcO were similar, we estimate that a large excess (> 40 equiv.) of **PPA** would be required to be added to replace the majority (> 90%) of AcO. However, only two equivalents of **PPA** (per AcO) are sufficient to replace most of AcO due to the high priority of **PPA** in co-ligand exchange. Thus, the result of Fig. 1d and Fig. S15 are consistent.
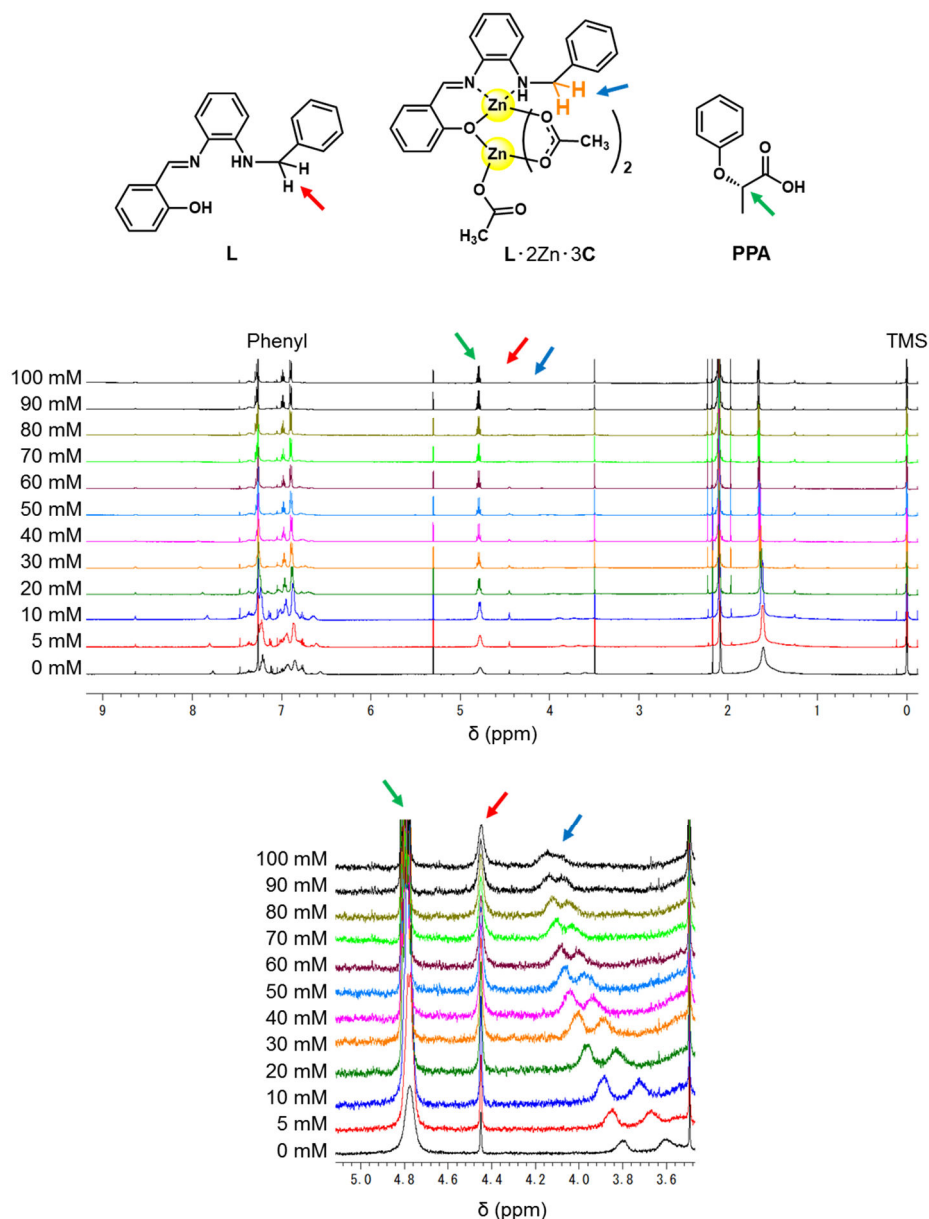
Figure S15. ^{1}H-NMR spectra (in CDCl$_3$, 25 ºC, 500 MHz) of **L·2Zn·3C** and (*S*)-**PPA** (4 mM) upon titration of acetic acid (0−100 mM). [**L**]$_{total}$ = 1 mM, [Zn^{2+}]$_{total}$ = 2 mM

25
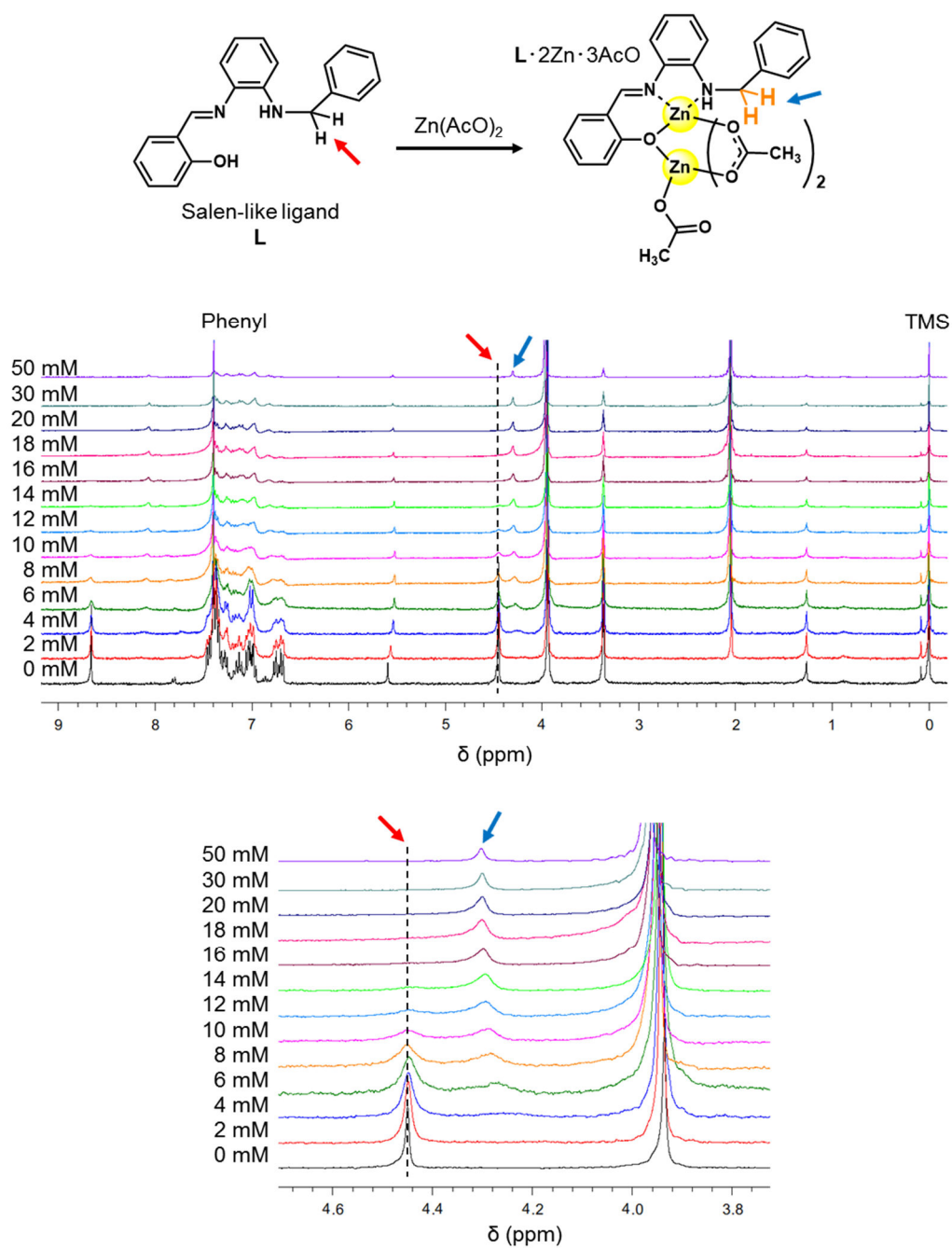
Figure S16. ^{1}H-NMR spectra of **L** (10 mM) in the presence of zinc acetate (0−50 mM) in CDCl$_3$/CD$_3$OD (4/1, 25 °C). A solution of **L** (10 mM) in CDCl$_3$/CD$_3$OD (4/1) was treated with a solution of zinc(II) acetate dihydrate (250 mM) in CD$_3$OD.
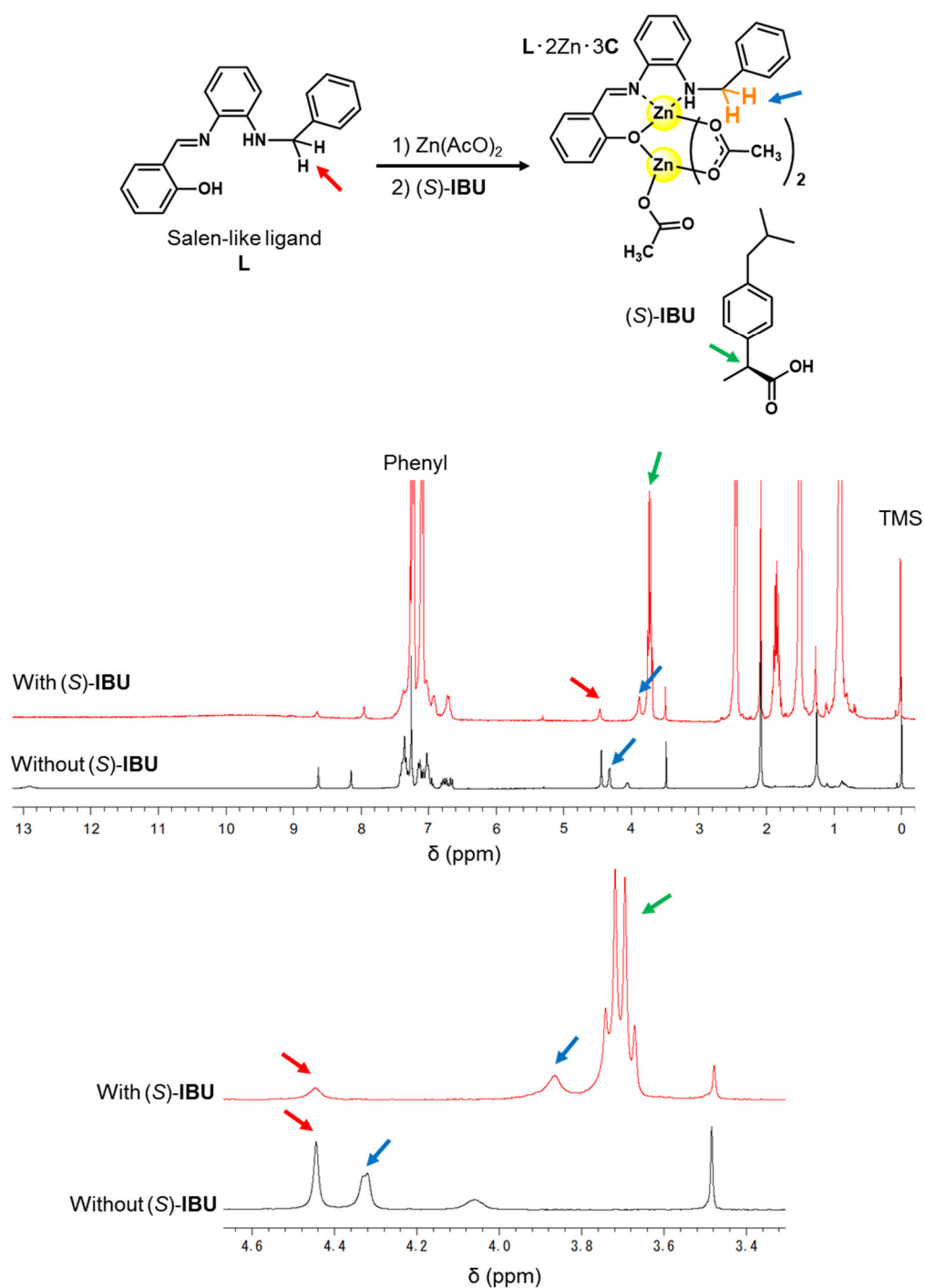
Figure S17. ^{1}H-NMR spectra of **L·2Zn·3C** in the presence and absence of (*S*)-2-(4-isobutylphenyl)propanoic acid ((*S*)-**IBU**) (100 mM) measured in CDCl$_3$ (25 ºC). [**L**]$_{total}$ = 10 mM
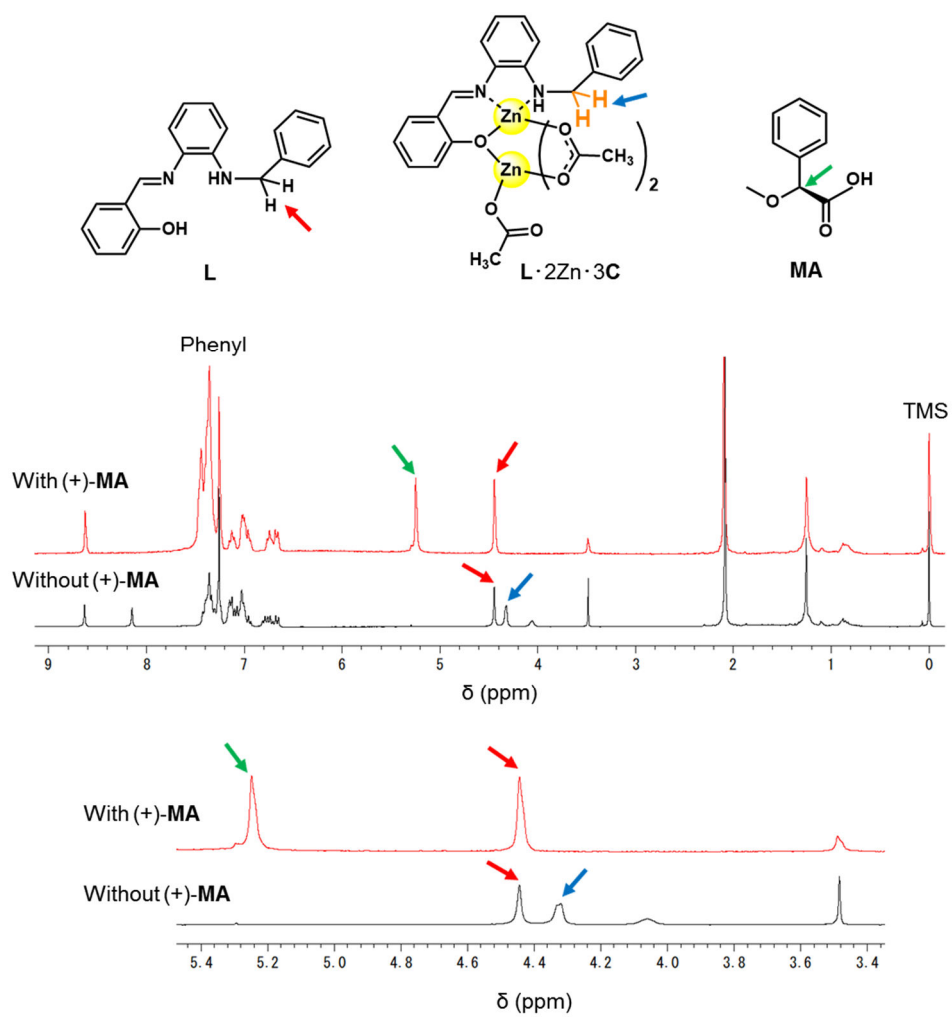
Figure S18. ^{1}H-NMR spectra of **L**·2Zn·3**C** in the presence and absence of (+)-mandelic acid ((+)-**MA**) (100 mM) measured in CDCl$_3$ (25 ºC). [**L**]$_{total}$ = 10 mM
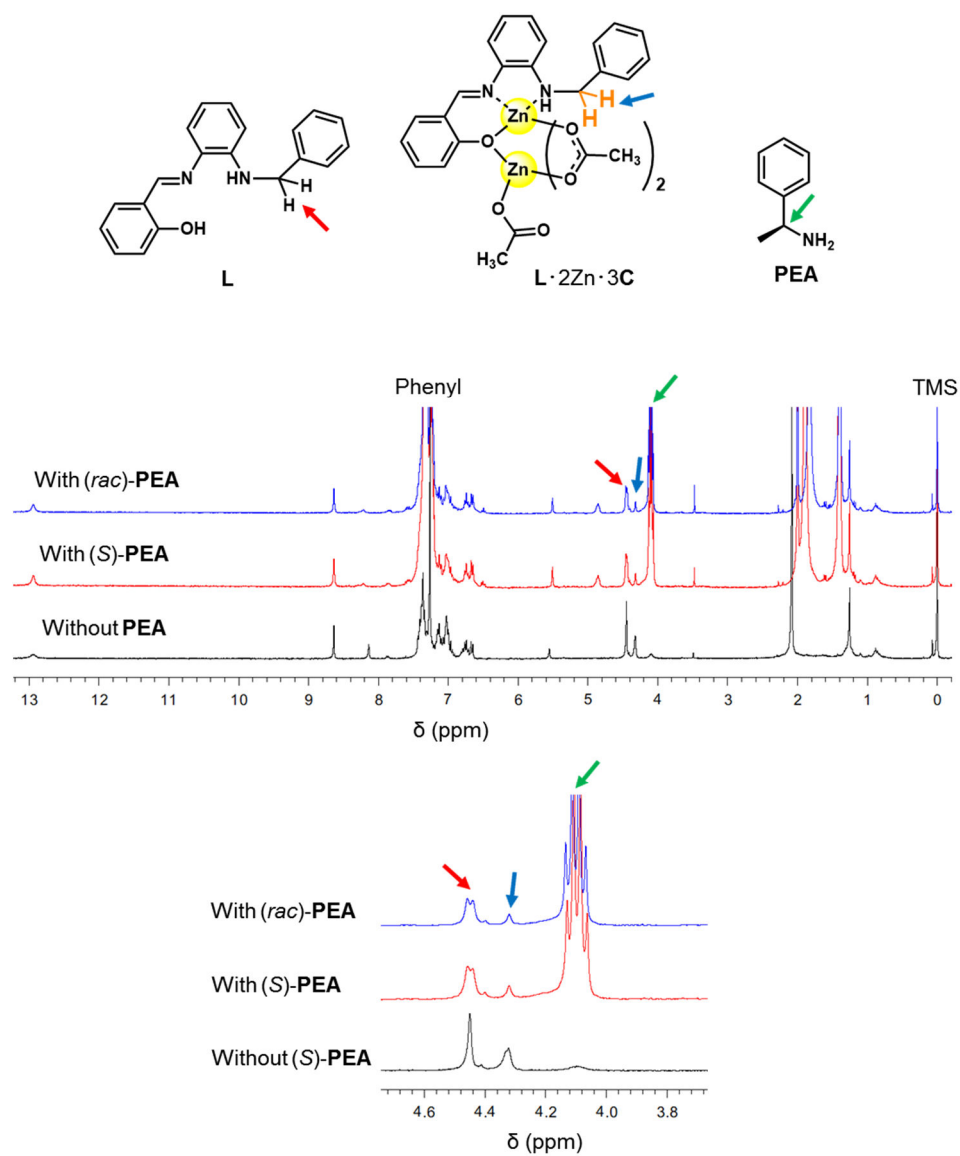
Figure S19. ¹H-NMR spectra of **L·2Zn·3C** in the presence and absence of (*S*)- or (*rac*)-1-phenylethylamine ((*S*)- or (*rac*)-**PEA**) (100 mM) measured in CDCl₃ (25 ºC). [**L**]total = 10 mM
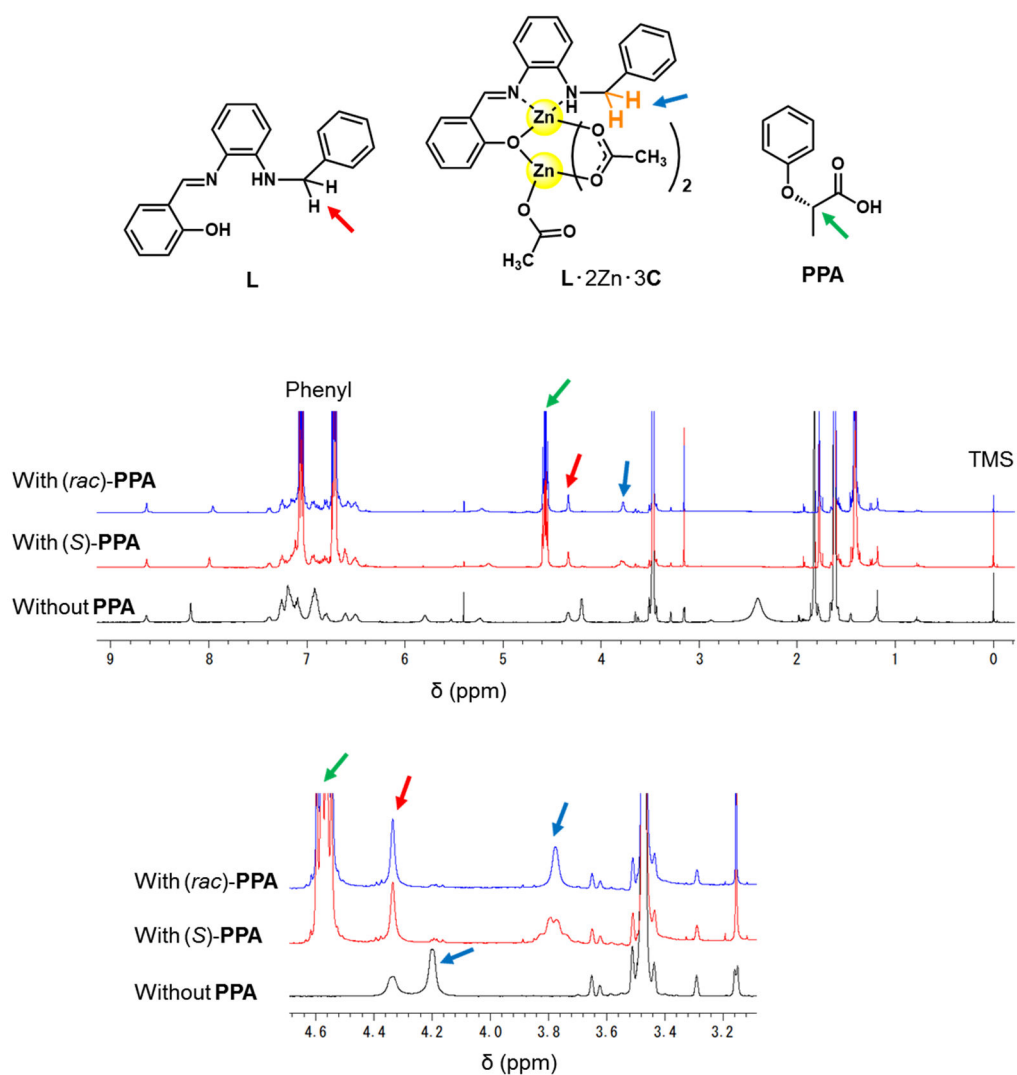
Figure S20. ^{1}H-NMR spectra of **L·2Zn·3C** in the presence and absence of (*S*)- or (*rac*)-**PPA** (80 mM) measured in tetrahydrofuran-d$_8$ (25 °C). [**L**]$_{total}$ = 10 mM
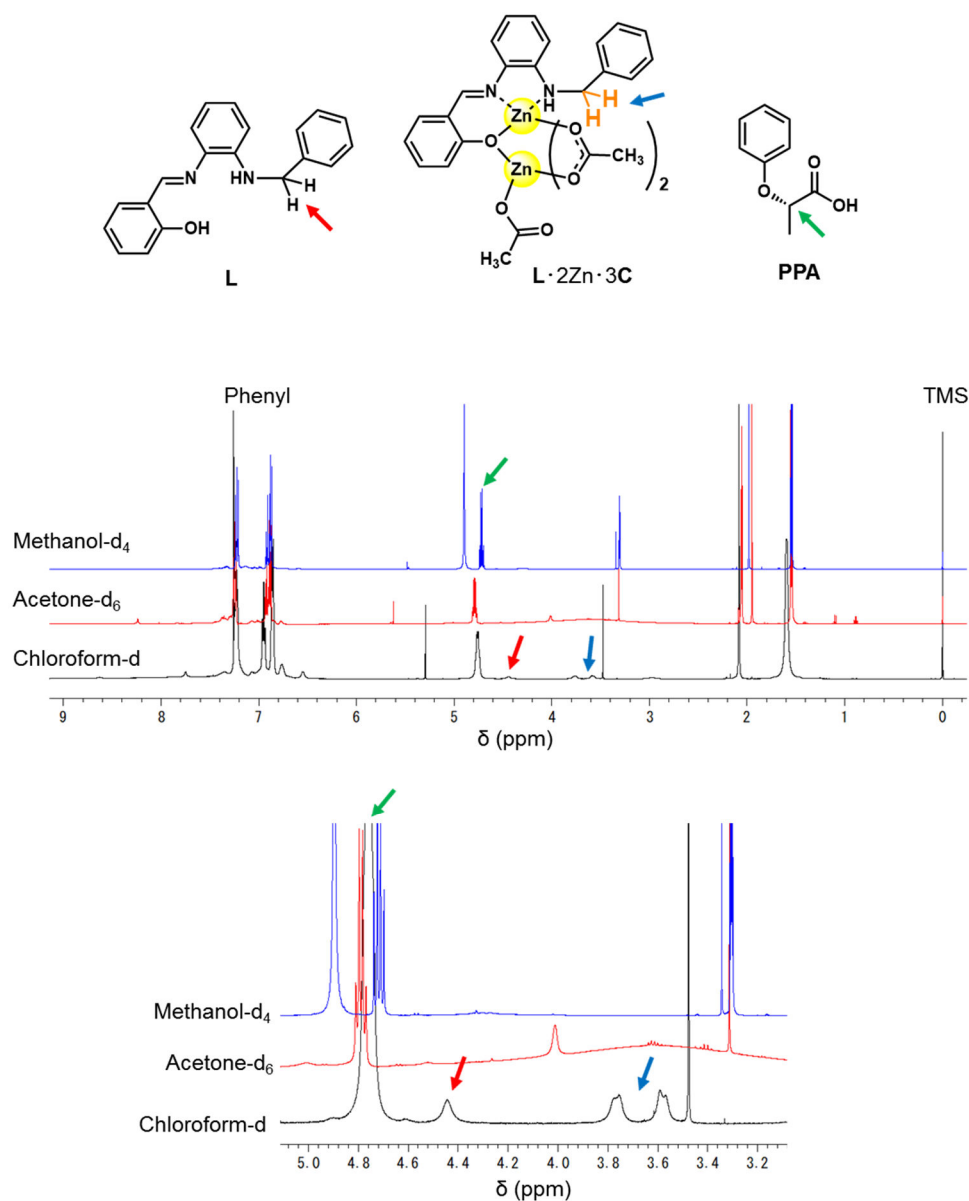
Figure S21. ¹H-NMR spectra of **L·2Zn·3C** in the presence of (*S*)-**PPA** (80 mM) measured in chloroform-d (CDCl₃), acetone-d₆, or methanol-d₄ (25 ºC, 500 MHz). [**L**]$_{total}$ = 10 mM. NMR signals of metal-ligand complex in acetone-d₆, or methanol-d₄ were too broad to observe due to coordination of solvents to the complex and/or slow co-ligand exchange.

5. CD spectra
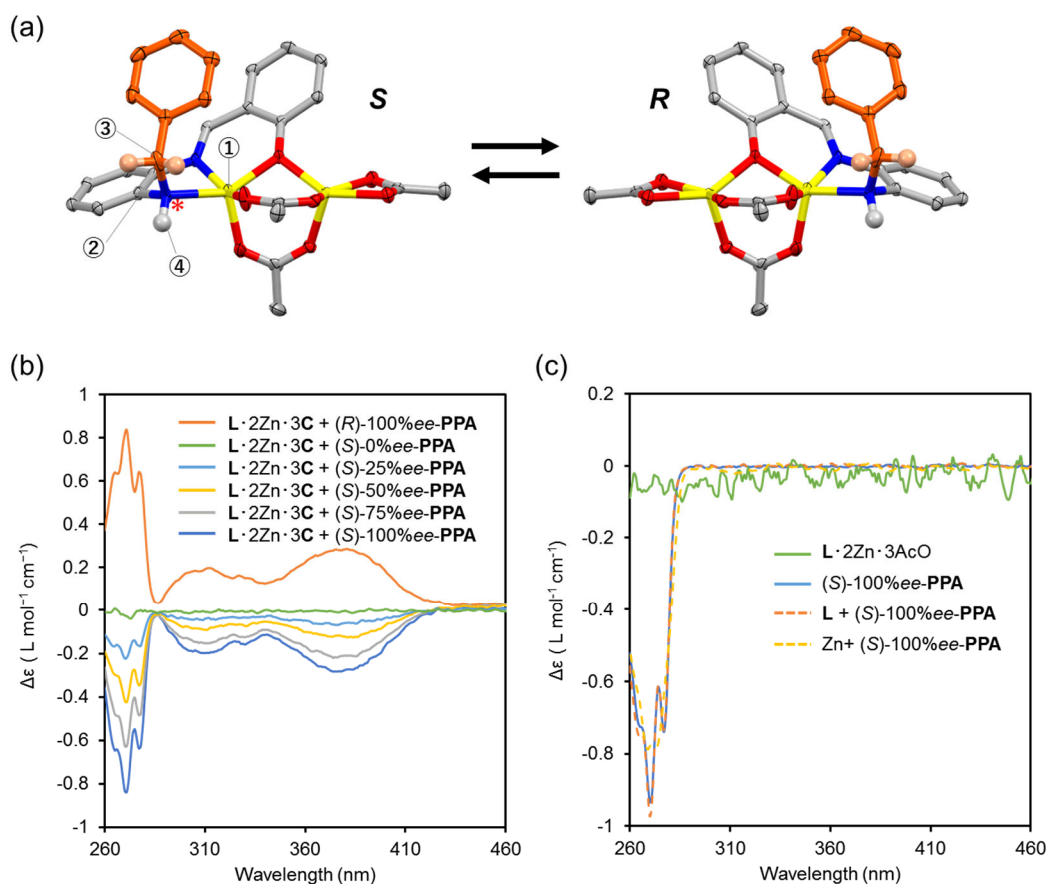
Figure S22. (a) Chirality in the crystal structure of zinc complex of **L**, showing two non-superimposable enantiomers. Chirality was assigned based on configuration at benzylic nitrogen atom (shown by asterisk). (b) CD spectra (in CDCl$_3$, 25°C) of **L·2Zn·3C** ([**L**]$_{total}$ = 1 mM) in the presence of **PPA** (8 mM) with various *ee*. A quartz cell with 1 mm path length was used. Molar circular dichroism ($\Delta\varepsilon$) was calculated based on the concentration of **PPA**. (c) CD spectra (in CDCl$_3$, 25°C) of **L·2Zn·3AcO** ([**L**]$_{total}$ = 1 mM), (*S*)-**PPA** (8 mM), the mixture of **L** (1 mM) and (*S*)-**PPA** (8 mM), and the mixture of zinc acetate (2 mM) and (*S*)-**PPA** (8 mM), showing no CD signals for wavelengths higher than 300 nm. When **PPA** is involved, molar circular dichroism ($\Delta\varepsilon$) was calculated based on the concentration of **PPA**. Molar circular dichroism ($\Delta\varepsilon$) of **L·2Zn·3AcO** was calculated based on the concentration [**L**]$_{total}$ = 1 mM.

6. Binding model and its analysis

6.1 Justification of the binding model and its manifestation in NMR and UV-Vis spectra

In order to investigate coordination of $Zn(AcO)_2$ with **L**, we performed NMR and UV-Vis titrations. During the NMR titration, ^{1}H-NMR signals due to free **L** gradually disappeared, and new ^{1}H NMR signals ascribed to the zinc complex emerged (Fig. S16 and S23). Thus, exchange between free **L** and **L** in the complex is slow on the NMR timescale. NMR signals of the free ligand were absent after addition of two equiv. of $Zn(AcO)_2$, and the binding isotherm, obtained from integrals due to free **L** and Zn^{2+}-complexed **L**, was almost linear (up to 2 equiv. of $Zn(AcO)_2$) due to strong binding (Fig. S23b). For UV-Vis titration, the spectrum of **L** gradually changed upon addition of $Zn(AcO)_2$ (Fig. S23c). From the NMR and UV-Vis titration experiments and singular value decomposition (SVD) analysis[11] the following host-guest binding model was adopted:

$$M + M \underset{}{\overset{K_{M2}}{\rightleftharpoons}} M_2$$

$$L + M \underset{}{\overset{K_{LM}}{\rightleftharpoons}} LM$$

$$L + M_2 \underset{}{\overset{K_{LM2}}{\rightleftharpoons}} LM_2$$
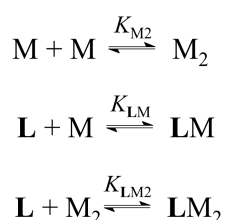
where the host is denoted as **L** and guest ($Zn(AcO)_2$) is denoted as M, **LM** denotes $L{\cdot}Zn{\cdot}AcO$ complex and **LM**$_2$ denotes $L{\cdot}2Zn{\cdot}3AcO$ complex. K_{M2}, K_{LM} and K_{LM2} are the equilibrium binding constants for the formation of M_2 dimer, **LM** and **LM**$_2$ complexes, respectively. This 1:2 binding model is supported by the X-ray crystal structure analysis (Fig. 3).

SVD analysis was used to identify the number of components (forms of host molecule) present in solution during the UV-Vis titration experiment. In this case, SVD yields three forms of host molecule (i.e., **L**, **LM** and **LM**$_2$) (Figs. S24-S25). This model also incorporates acetate-bridged Zn^{2+} dimer (M_2) formation with subsequent complexation to host **L** (forming **LM**$_2$ complex). Simultaneous fitting of the NMR and UV-Vis binding isotherms (Figs. S23b,d) together with analysis of the model (Fig. S26) yields the following values of binding constants: $K_{LM2} = (1.8 \pm 0.1) \times 10^4$ M^{-1}, $K_{LM} \geq 5 \times 10^4$ M^{-1} and $K_{M2} \geq 9.5 \times 10^5$ M^{-1}. Only lower bounds can be determined for K_{LM} and K_{M2} because the 1:1 **L**:M complex cannot be clearly observed using NMR or UV-Vis spectroscopy. There are slight shifts and broadening of the resonances in the NMR spectrum at 4.3 ppm up to 10 mM (1 equiv.) of $Zn(AcO)_2$ (Fig. S23a) suggesting an intermediate rate of exchange between **LM** and **LM**$_2$ complexes. However, direct evaluation of the content of **LM** is not possible, so that **LM** and **LM**$_2$ species are treated as a sum in the experimental binding isotherm. The speciation diagrams (in Fig. S27) suggest that the maximum content of host in the **LM** complex is only 16.3% (at around 1 equiv. of M). This is in agreement with NMR and UV-Vis observations. Details of the derivation of the binding model and its fitting to the experimental data and analysis of obtained results with all the implications are discussed in the following sections.
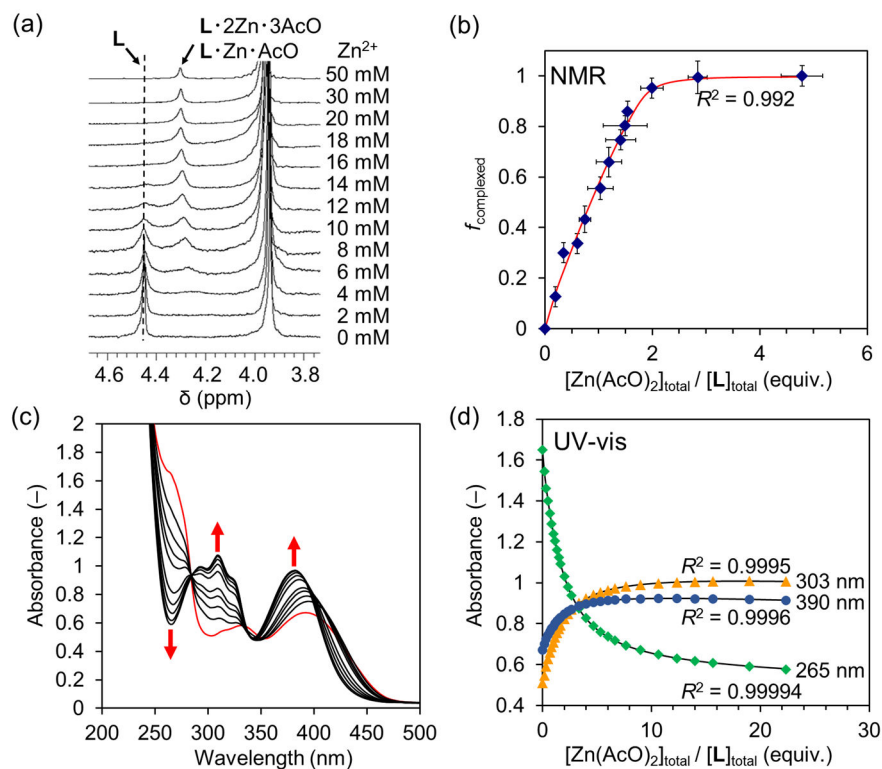
Figure S23. (a) ^{1}H-NMR titration of **L** (10 mM) with $Zn(AcO)_2$ (0−50 mM) in $CDCl_3/CD_3OD$ (4/1) at 25˚C. Zinc(II) acetate dihydrate (250 mM) in CD_3OD was used for titration. (b) Plot of fraction of complexed host (**L**M, **L**M$_2$) as obtained from NMR (blue diamonds) and fitting of binding isotherm (red line) using the model described in the text and the following section. $f_{complexed}$ is fraction of complexed host (**L**M, **L**M$_2$). (c) UV-Vis titration of **L** (0.1mM) with $Zn(AcO)_2$ (0−2.2 mM) in $CHCl_3/MeOH$ (4/1) at 25˚C. Zinc(II) acetate dihydrate (50 mM) in MeOH was used for titration. (d) Fitting of binding isotherms (gray lines) obtained from UV-Vis titration at 25˚C.

6.2 SVD decomposition of UV-vis titration of L with zinc acetate

The singular value decomposition (SVD) method was used to determine the number of absorbing species, i.e. the number of forms of the host molecule present during titration. During titration experiments, only a few absorbing species are present in the spectra (e.g. free host, complex 1:1, complex 1:2, etc.). Spectra (absorbance values) obtained during a titration experiment can be arranged in a $N_{res} \times N_{exp}$ matrix $\mathbf{A}$, where N_{exp} is the number of titration steps and N_{res} is the number of discrete points comprising each spectrum.

Assuming that the spectral shape of these absorbing species is constant during the entirety of the experiment, matrix $\mathbf{A}$ can be viewed as a linear combination of the matrices of the absorbing species' spectra. This linear combination is expressed as a matrix product:

$$\mathbf{A}_{\lambda n} = \sum_{i=1}^{N_{spec}} \mathbf{Z}_{\lambda i}\, \mathbf{F}_{in} \tag{S1}$$

where $\lambda = 1, 2 \dots N_{res}$ and $n = 1, 2, \dots N_{exp}$.

Columns of the matrix $\mathbf{Z}$ contain spectral shapes of the individual absorbing species and rows of $\mathbf{F}$ contain their fractions during experiment (each column of $\mathbf{F}$ sums to unity). N_{spec} denotes the number of absorbing species present (for example: $N_{spec} = 3$ if only free host H, complex 1:1 and complex 1:2 are present). The correct value of N_{spec} can be deduced from the *singular value decomposition* (SVD)[11] procedure applied to the matrix $\mathbf{A}$:

$$\mathbf{A}_{\lambda n} = \sum_{\mu=1}^{N_{res}} \sum_{m=1}^{N_{exp}} \mathbf{U}_{\lambda\mu} \mathbf{W}_{\mu m} \mathbf{V}_{mn} \tag{S2}$$

where again $\lambda = 1, 2 \dots N_{res}$ and $n = 1, 2, \dots N_{exp}$.

The columns of the square orthonormal $N_{res} \times N_{res}$ matrix $\mathbf{U}$ are called basis spectra. $\mathbf{W}$ is a rectangular diagonal $N_{res} \times N_{exp}$ matrix. The diagonal elements of $\mathbf{W}$ are denoted as singular values and are sorted in descending order. Rows of the square orthonormal $N_{res} \times N_{res}$ matrix $\mathbf{V}$ are called amplitude vectors. A convenient compact form of SVD is $\mathbf{A} = \mathbf{UK}$ (where $\mathbf{K} = \mathbf{WV}$), where rows of $\mathbf{K}$ are called *combination coefficients*.

In the presence of N_{spec} absorbing species in the titration experiment, the first N_{spec} basis spectra carry information about spectral shape of the absorbing species and the first N_{spec} amplitude vectors (or combination coefficients) carry information about their fractions in the sample during the experiment. Remaining components of the matrices $\mathbf{U}$ and $\mathbf{V}$ or $\mathbf{K}$ represent noise. Using an approximate transformation matrix, the basis spectra can be transformed into the matrix of absorbing spectra $\mathbf{Z}$ and amplitude vectors/combination coeff. into the matrix of fractions $\mathbf{F}$[11a, 11c, 11d,S9] The presence of N_{spec} absorbing species causes the first N_{spec} singular values to be substantially higher than the rest (this holds for sufficiently high signal/noise ratio; N_{spec} is often denoted as the *factor dimension*). Another indicator is a plot of residuals that describes average standard error of the SVD approximation of measured spectra for given factor dimension. Residuals are defined as follows:[11b]

$$\text{residual}(i) = \sqrt{\left.\sum_{j=i+1}^{N_{exp}} \mathbf{W}_{jj}^2 \middle/ N_{res}(N_{exp} - i)\right.} \tag{S3}$$

For $i = N_{spec}$ the value of the residual usually drops significantly (or has a very low value) since all relevant spectra of absorbing species are included in the SVD approximation of $\mathbf{A}$. For $i > N_{spec}$ the value of the residual does not vary much since only basis vectors which consist mostly of noise are added into the SVD approximation. Signal containing basis and amplitude vectors also tend to have higher autocorrelation compared

to noise-containing vectors. The simplest case $N_{spec} = 2$ can be easily identified by observing a plot of mutual dependence of the first two combination coefficients, which should be linear.[S10] In our analysis of titration of **L** with $Zn(AcO)_2$, it can be seen that this dependence is not linear (Fig. S24f) indicating the presence of more than two absorbing species (i.e. more than two forms of host molecule **L**). From overall results of the SVD analysis (Fig. S24), it can be concluded that spectra of three significant species are present in the UV-Vis absorption spectra, which correspond to free host **L** , **L·Zn·AcO** (=**LM**) and **L·2Zn·3AcO** (=**LM₂**) species.
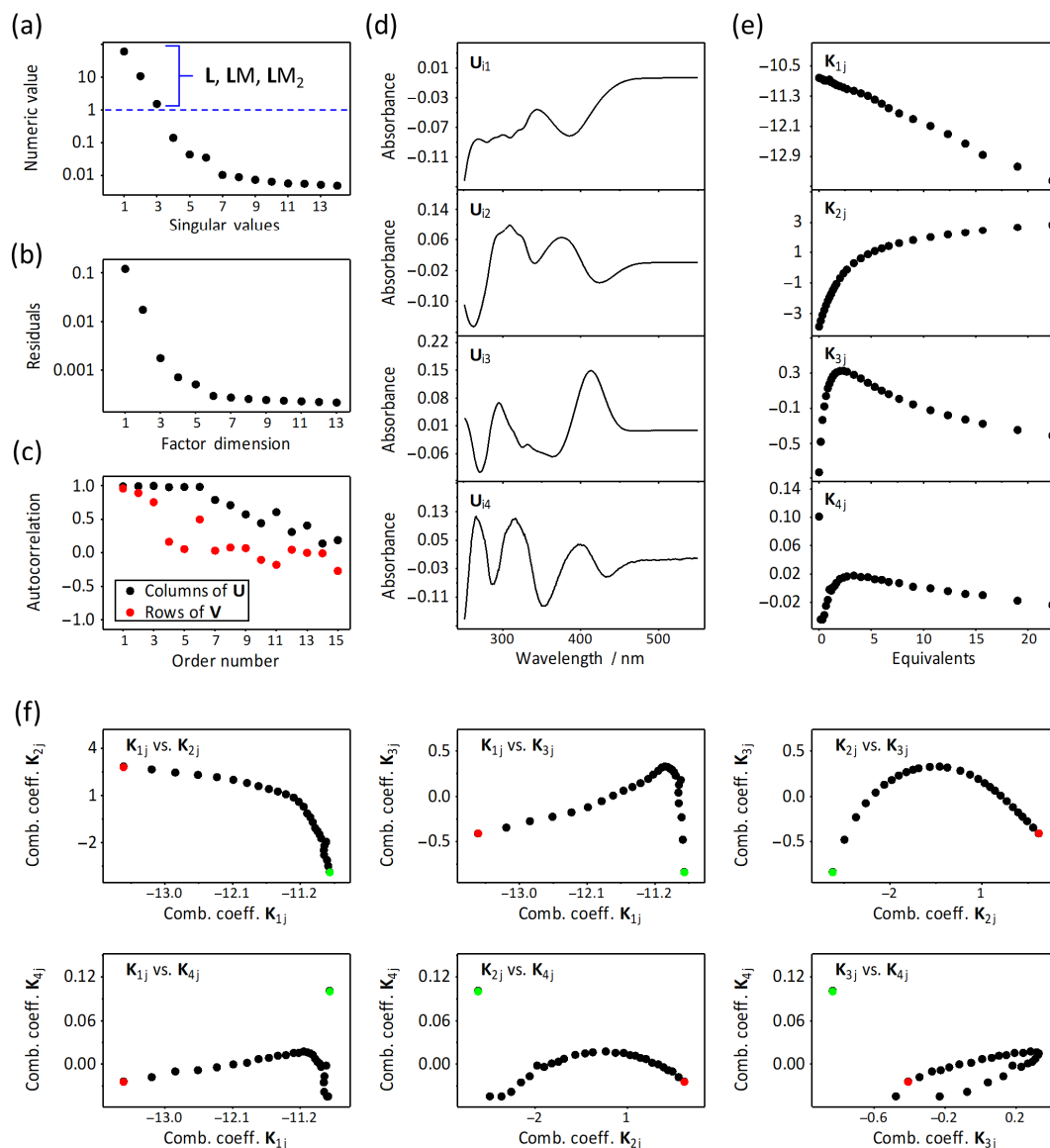
Figure S24: SVD decomposition of UV-vis titration of **L** ($CHCl_3/MeOH = 4/1$, 3 mL, 25°C) with 0-19 equiv. $Zn(OAc)_2$ (guest M). For actual UV-vis spectra see Fig. 23c (a) Singular values indicating the presence of three species, i.e. free host (**L**) and two complexed forms of host (**LM** and **LM₂**). (b) Residuals (at factor dimension = 3 the residual "error" is small). (c) Autocorrelations of basis **U** and amplitude vectors **V**, respectively. (d) First four basis vectors **U**. (e) First 4 amplitude vectors. (f) Mutual dependence of first four combination coefficients (green and red dots denote first and last measured spectrum, respectively).
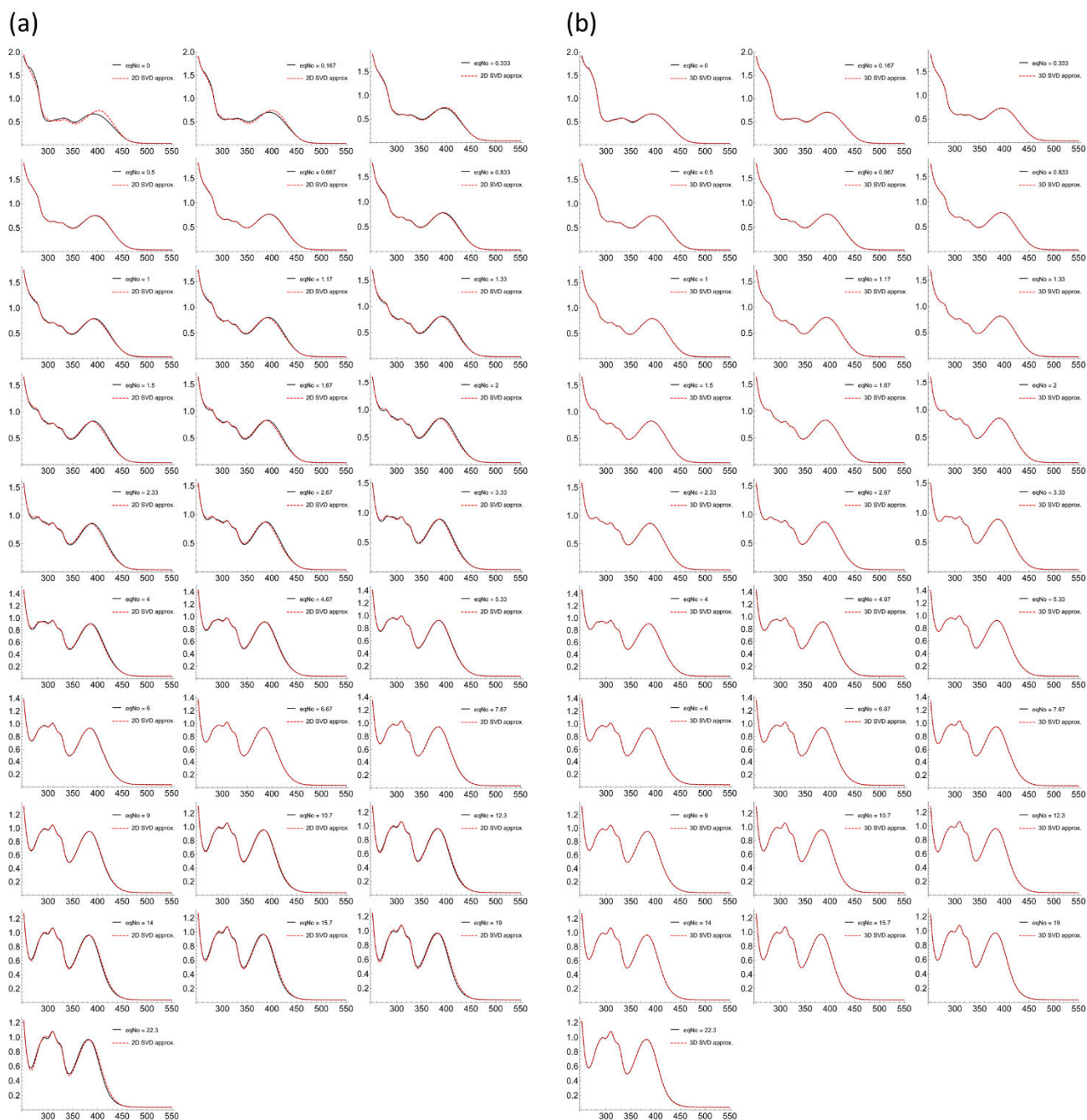
Figure S25: Individual UV-vis spectra from titration of host (**L**) (0.1mM) with guest (M) $Zn(OAc)_2$ in CHCl$_3$/MeOH (4/1) at 25˚C (see Fig. 23c) reconstructed using (a) two basis vectors (i.e. 2D SVD approximation) and (b) three basis vectors (i.e. 3D SVD approximation). High accuracy of reconstruction of original UV-vis spectra can be seen when 3D SVD approximation is used (black line = original spectrum, red dashed line = SVD approximation).

6.3 Derivation of binding model

We have adopted the following binding model based on SVD analysis of UV-Vis spectra (Figs. S24 and S25) and the apparent saturation of NMR binding isotherm at 2 equiv. of guest (zinc acetate) (Fig. 23b) together with the stoichiometry of **L**·2Zn·3AcO complex found in its crystal structure (Fig. 3).

The binding interaction between host (**L**) and guest M ($Zn(OAc)_2$) is described by the following equilibrium Equations S4-S6.

$$M + M \xrightleftharpoons{K_{M2}} M_2 \tag{S4}$$

$$\mathbf{L} + M \xrightleftharpoons{K_{LM}} \mathbf{LM} \tag{S5}$$

$$\mathbf{L} + M_2 \xrightleftharpoons{K_{LM2}} \mathbf{LM_2} \tag{S6}$$
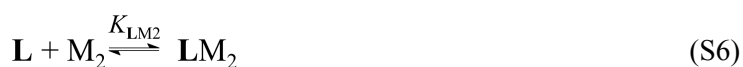
Where K_{M2} is the equilibrium dimerization binding constant of M_2 dimer formation, K_{LM} is the equilibrium binding constant of **LM** complex formation and K_{LM2} is the equilibrium binding constant of **LM$_2$** complex formation. Then the following formulas hold for binding constants and mass balances:

$$K_{M2} = \frac{[M_2]}{[M]^2} \tag{S7}$$

$$K_{LM} = \frac{[\mathbf{LM}]}{[\mathbf{L}][M]} \tag{S8}$$

$$K_{LM2} = \frac{[\mathbf{LM_2}]}{[\mathbf{L}][M_2]} \tag{S9}$$

$$[\mathbf{L}]_t = [\mathbf{L}] + [\mathbf{LM}] + [\mathbf{LM_2}] \tag{S10}$$

$$[M]_t = [M] + [\mathbf{LM}] + 2[\mathbf{LM_2}] + 2[M_2] \tag{S11}$$

Where $[\mathbf{L}]_t$ and $[M]_t$ are the total analytical concentrations of **L** and M, respectively. Square brackets "[ ]" denote the concentrations of indicated species. Expression of the $[M_2]$, $[\mathbf{LM}]$ and $[\mathbf{LM_2}]$ terms from Equations S7, S8 and S9, respectively, and substitution in Equations S10 and S11 yields the following formulas:

$$[\mathbf{L}]_t = [\mathbf{L}] + K_{LM}[\mathbf{L}][M] + K_{M2}K_{LM2}[\mathbf{L}][M]^2 \tag{S12}$$

$$[M]_t = [M] + K_{LM}[\mathbf{L}][M] + 2K_{M2}K_{LM2}[\mathbf{L}][M]^2 + 2K_{M2}[M]^2 \tag{S13}$$

Expression of the term [**L**] from Equation S12 gives Equation S14.

$$[\mathbf{L}] = \frac{[\mathbf{L}]_t}{1 + K_{LM}[M] + K_{M2}K_{LM2}[M]^2} \tag{S14}$$

Substitution of [**L**] from Equation S14 into Equation S13 yields (after some rearrangements) the formula for

[M] in the form of a fourth order algebraic equation (Equation S15).

$$
\begin{aligned}
&2K_{M2}^2 K_{LM2}[M]^4 + K_{M2}(2K_{LM} + K_{LM2})[M]^3 \\
&+\big(2K_{M2} + K_{LM} + K_{M2}K_{LM2}(2[L]_t - [M]_t)\big)[M]^2 \\
&+\big(1 + K_{LM}([L]_t - [M]_t)\big)[M] - [M]_t = 0
\end{aligned}
\tag{S15}
$$

Solution of Equation S15 using a numerical bisection method in the interval $[M] \in [0, [M]_t]$ yields the concentration of free guest [M]. The concentrations of other species, such as [L], [M₂], [LM] and [LM₂] can be obtained by subsequent evaluation of Equations S14, S7, S8, and S9, respectively. The theoretical NMR (Equation S16) and UV-vis (Equation S17) binding isotherms have the following forms.

$$
f_{complexed} = ([LM] + [LM_2])/[L]_t \tag{S16}
$$

$$
A = \varepsilon_L d[L] + \varepsilon_{LM} d[LM] + \varepsilon_{LM2} d[LM_2] \tag{S17}
$$

Where $f_{complexed}$ is the fraction of complexed host **L** (i.e. [LM] and [LM₂]) observed in NMR. The experimental binding isotherm $f_{complexed}^{exp}$ is constructed as the ratio of integrated intensity of the resonance at 4.30 ppm to integrated intensities (I_{ppm}) of both resonances at 4.30 ppm and 4.44 ppm, i.e. $f_{complexed}^{exp} = I_{4.30} / (I_{4.30} + I_{4.44})$ (Fig. 23a). A is the UV-vis absorbance at a particular wavelength (three wavelengths were selected 265, 303 and 390 nm). The ε_L, ε_{LM} and ε_{LM2} are the molar extinction coefficients of **L**, **LM** and **LM₂**, respectively. The value of d is path length (1 cm). One NMR isotherm and three UV-vis binding isotherms expressed in Equations S16 and S17 were fitted simultaneously to experimental data (using a non-linear least squares fitting procedure).

6.4 Analysis of the results obtained from the binding model

Analyses of the binding properties of host molecule **L** with guest M (Zn(OAc)₂) were performed (as mentioned above) by simultaneous fitting of NMR and UV-vis binding isotherms. This approach includes behaviour of the system at high (NMR) and low (UV-vis) concentrations.

SVD analysis yields the presence of **L** in three forms (**L**, **LM** and **LM₂**). The **LM** form is not clearly observable by either of the two experimental methods (NMR or UV-Vis). There is a slight drift and broadening of the NMR resonance at 4.3 ppm up to 10 mM (1 equiv.) of Zn(OAc)₂ (Fig. 23a) suggesting an intermediate rate of exchange between the **LM** and **LM₂** complexes. However, the direct evaluation of **LM** content of is not possible. Therefore, the NMR binding isotherm (Equation S16) contains both **LM** and **LM₂** species, since they are undistinguishable. In order to account for this problem, simultaneous fitting of both NMR and UV-Vis experimental binding isotherms was performed for a broad range of K_{LM} values. At each value of K_{LM}, the best fit was found and the measure of its quality represented as the *total sum of squares* (TSS) was determined (Fig. S26a) together with the corresponding binding constants K_{LM2} and K_{M2} as seen in Figs S26b and S26c, respectively. The plot of TSS vs. K_{LM} (Fig. 26a) has a region denoted by a gray background with satisfactory quality of the fit (i.e. acceptable TSS values). This region does not have an upper boundary for K_{LM} values. However, there is a clear lower boundary where the TSS values rapidly grow. When the corresponding values of K_{LM2} and K_{M2} after each fitting

procedure are plotted vs. K_{LM} (as seen in Figs. S26b and S26c), it can be seen that the K_{LM2} is a constant (in the region with acceptable TSS values) while the K_{M2} dependence has the form of a power law $K_{M2} \sim K_{LM}^{\alpha}$. From these plots, the following conclusions regarding the values of equilibrium binding constants can be formulated (Equations S18-S20).

$$K_{\mathbf{LM2}} = (1.8 \pm 0.1) \times 10^4 \ \text{M}^{-1} \tag{S18}$$

$$K_{\mathbf{LM}} \geq 5 \times 10^4 \ \text{M}^{-1} \tag{S19}$$

$$K_{\mathbf{M2}} = 3.78 \times 10^{-4} \ K_{\mathbf{LM}}^2 \tag{S20}$$

These equations also yield the minimum value of $K_{M2}(\text{min}) = 9.45 \times 10^5$ M^{-1} derived by combining Equations S19 and S20. Equation S20 is a simple mutual relationship between K_{M2} and K_{LM} in the form of second power (i.e. power law function). The ambiguity in the missing exact determination of K_{M2} and K_{LM} values arises from the inability to observe directly the **LM** complex in the (NMR or UV-Vis) spectral data.
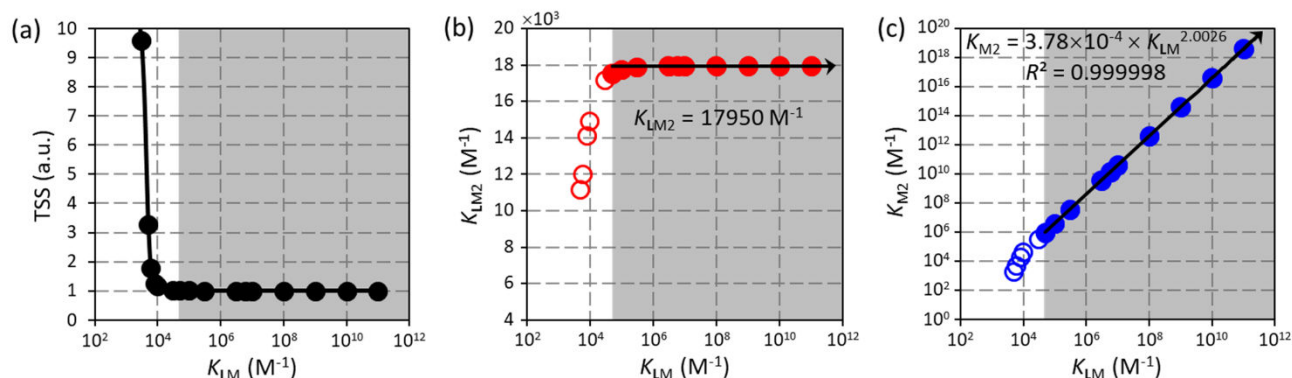

Figure S26. Results of simultaneous NMR and UV-vis data fitting analysis of host **L** with guest M (Zn(OAc)$_2$) with variable K_{LM}. (a) Plot of total sum of squares (TSS) dependence on K_{LM}. (b) Lin-log plot of K_{LM2} dependence on K_{LM}. (c) Log-log plot of K_{M2} dependence on K_{LM} (log-log plot is used to emphasize the presence of power law). Gray regions denote acceptable TSS values. The black arrows in (b) and (c) show the best linear fit with corresponding equation given in the graph.

6.5 Binding model – speciation diagrams

In the region with acceptable TSS values (defined by Equations S18-S20), the speciation diagrams (Fig. S27) can be constructed using the above analyses of the binding model. The diagrams remain unchanged in this region (within 1% relative error in the fractions of species). In the Fig. S27b,e, it can be seen that the fraction of host molecule **L** in the form of **LM** complex (f_{LM}) is always $f_{LM} \leq 0.163$ with a maximum close to $[M]_t/[L]_t$ = 1 equiv. This low content of **LM** complex is in agreement with NMR and UV-Vis observations (i.e. **LM** cannot be clearly observed in spectra due to its low content). However, the SVD analysis of the UV-Vis titration suggests the presence of small amounts of this third species **LM** (Fig. S24a), which yields a complete picture of the complexation process between **L** and Zn(OAc)$_2$.
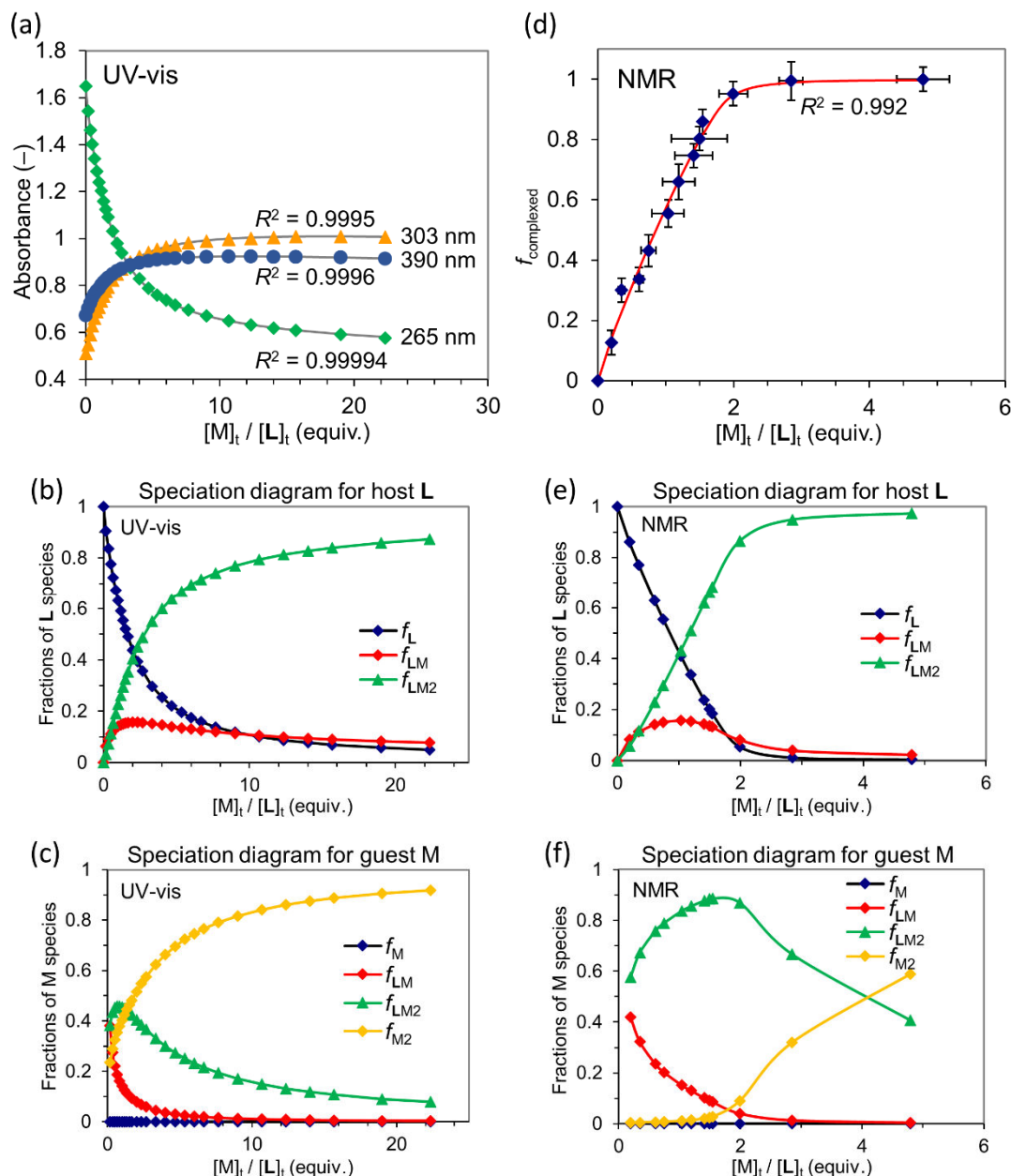
Figure S27: (a) Fitting of the UV-vis binding isotherms obtained from titration experiments at 265, 303 and 390 nm using Equation S17. $[\mathbf{L}]_t = 0.1$ mM. (b) Speciation diagrams for host molecule $\mathbf{L}$ as obtained from UV-vis titration. (c) Speciation diagrams for guest molecule M ($Zn(OAc)_2$) as obtained from UV-vis titration. (d) Fitting of the NMR binding isotherms obtained from titration experiments using Equation S16. $[\mathbf{L}]_t = 10$ mM. (e) Speciation diagrams for host molecule $\mathbf{L}$ as obtained from NMR titration. (f) Speciation diagrams for guest molecule M ($Zn(OAc)_2$) as obtained from NMR titration. Notes: The binding constant used for construction of these speciation diagrams are: $K_{M2} = 9.45 \times 10^5$ M^{-1}, $K_{LM} = 5.00 \times 10^4$ M^{-1} and $K_{LM2} = 1.75 \times 10^4$ M^{-1} (i.e. the minimum possible values allowed by Equations S18-S20). The fractions f are calculated in the following way. Speciation diagrams for host $\mathbf{L}$: $f_{\mathbf{L}} = [\mathbf{L}]/[\mathbf{L}]_t$, $f_{LM} = [LM]/[\mathbf{L}]_t$, $f_{LM2} = [LM_2]/[\mathbf{L}]_t$. Speciation diagrams for guest M: $f_M = [M]/[M]_t$, $f_{LM} = [LM]/[M]_t$, $f_{LM2} = 2[LM_2]/[M]_t$, $f_{M2} = 2[M_2]/[M]_t$.

6.6 Analysis of binding selectivity of LM_2 complex to PPA and AcOH

We have estimated the binding affinity of **L·2Zn·3AcO** complex to 2-phenoxypropionic acid (**PPA**) over acetic acid (**AcOH**) using a competitive binding experiment. NMR titration of AcOH into a solution of **L·2Zn·3AcO** and 4 equiv. of (*S*)-**PPA** was performed (Fig. S15). The results of this experiment are plotted in Fig. S28. It can be seen that the complexed phenoxypropionate (**PP**) is replaced by AcOH and therefore the magnitude of splitting $\Delta\delta$ is decreasing (Fig. S28a). The position of the centre of the CH_2 group also shifts downfield (Fig. S28b).
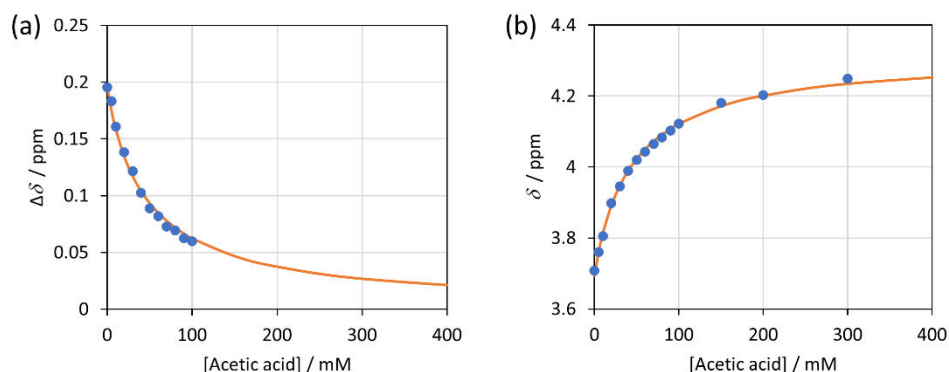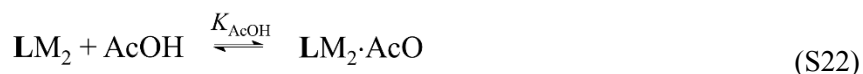

Figure S28. Analysis of titration experiment in Fig. S15 and determination of relative affinity of **PPA** over AcOH. Plot of (a) the magnitude of splitting $\Delta\delta$ of methylene CH_2 group and (b) position of its center δ during the titration of AcOH into the solution of **L·2Zn·3AcO** and 4 equiv. of (*S*)-**PPA** (in $CDCl_3$, 25 ºC). Key: Blue dots = experimental values, orange line = fit using competitive binding model. The fitting procedure yields selectivity ratio K_{PPA}/K_{AcOH} = 12.

In first approximation, these observations can be modelled using a competitive binding model expressed by the following equilibrium Equations S21 and S22:

$$LM_2 + PPA \quad \overset{K_{PPA}}{\rightleftharpoons} \quad LM_2 \cdot PP \tag{S21}$$

$$LM_2 + AcOH \quad \overset{K_{AcOH}}{\rightleftharpoons} \quad LM_2 \cdot AcO \tag{S22}$$

where K_{PPA} and K_{AcOH} are respectively equilibrium binding constants for **PPA** and AcOH to **L·2Zn·3AcO** (**LM₂**) complex. During the binding process a proton is exchanged between **PP** and AcOH (or **PPA** and AcO). The solution of this model can be found in the Supporting information of Ref. 2d of the main manuscript. The experimental data in Fig. S28 were fitted using this simple model which yields the selectivity ratio K_{PPA}/K_{AcOH} = 12. The actual values of binding constants cannot be precisely determined using this approximation, however the lower bound is located around $K_{PPA} \geq 10^5$ M⁻¹ and $K_{AcOH} \geq 8 \times 10^3$ M⁻¹. It is anticipated that these values are actually several orders of magnitude greater necessitated by charge balancing of the **L·2Zn·3C** complex (moreover, we always observe quantitative binding of co-ligand).

7. ESI-MS study

ESI-MS study (Figs. S29−S31) implies the formation of **L·2Zn·3PPA** in the mixture of **L·2Zn·3AcO** and **PPA**, although signals for the required ions are relatively weak (compared to other observed ion clusters and some unassignable species). It is difficult to conclude that ESI-MS spectra reflect the molecular species in solution and this is likely due to the ionization conditions applied.

Experimental	Theoretical	Compound	Chemical formula
423.0696	423.0682	**L·Zn·AcO**	$C_{22}H_{19}O_3N_2Zn$
605.0258	605.0239	**L·2Zn·3AcO**	$C_{26}H_{25}O_7N_2Zn_2$
684.8062	–	unknown	–
1088.6295	–	unknown	–
1130.6399	–	unknown	–

	Experimental	Theoretical
a	423.0696	423.0682
b	424.0728	424.0715
c	425.0663	425.0651
d	426.0689	426.0684
e	427.0647	427.0639
f	428.0686	428.0672

	Experimental	Theoretical
a	605.0258	605.0239
b	606.0294	606.0273
c	607.0226	607.0208
d	608.0245	608.0242
e	609.0209	609.0196
f	610.0232	610.0230
g	611.0186	611.0165
h	612.0209	612.0199
i	613.0170	613.0153
j	614.0212	614.0187

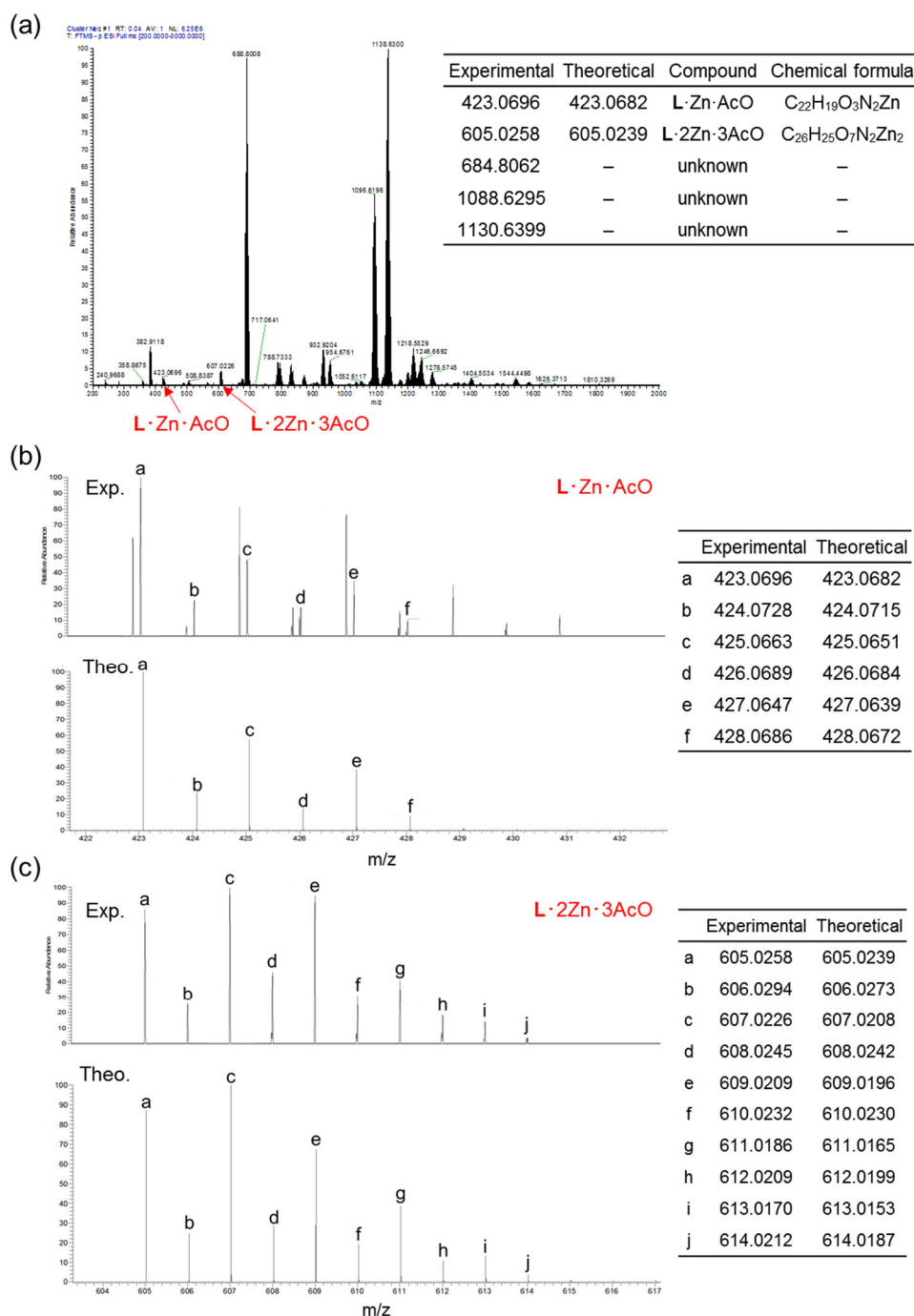**Figure S29.** (a) ESI-MS spectrum of **L·Zn·3AcO** in CDCl$_3$ (1 mM of **L** and 2 mM of zinc acetate) measured in negative-charge detection mode. Experimental and theoretical isotope signals for (b) **L·Zn·AcO** and (c) **L·2Zn·3AcO**, showing the consistency between experimental and calculated patterns.

43

(a)

Cluster with S-PPA Neg #1 RT: 0.04 AV: 1 NL: 1.04E7
T: FTMS - p ESI Full ms [200.0000-0000.0000]

2Zn·5PPA

Zn·3PPA

L·2Zn·3PPA

Experimental	Theoretical	Compound	Chemical formula
559.0952	559.0941	Zn·3PPA	$C_{27}H_{27}O_9Zn$
Not detected	711.0663	L·2Zn·2AcO·PPA	$C_{33}H_{31}O_8N_2Zn_2$
805.0828	–	unknown	–
823.0489	–	unknown	–
Not detected	817.1082	L·2Zn·AcO·2PPA	$C_{40}H_{37}O_9N_2Zn_2$
923.1514	923.1495	L·2Zn·3PPA	$C_{47}H_{43}O_{10}N_2Zn_2$
953.1354	953.1336	2Zn·5PPA	$C_{45}H_{45}O_{15}Zn_2$

(b)

Exp.

L·2Zn·3PPA

Theo.

m/z

	Experimental	Theoretical
a	923.1514	923.1495
b	924.1548	924.1529
c	925.1489	925.1464
d	926.1514	926.1498
e	927.1477	927.1452
f	928.1500	928.1486
g	929.1465	929.1421
h	930.1479	930.1455
i	931.1467	931.1409
j	932.1486	932.1443
k	933.1484	933.1476

(c)

807.0800
827.0443
795.0624
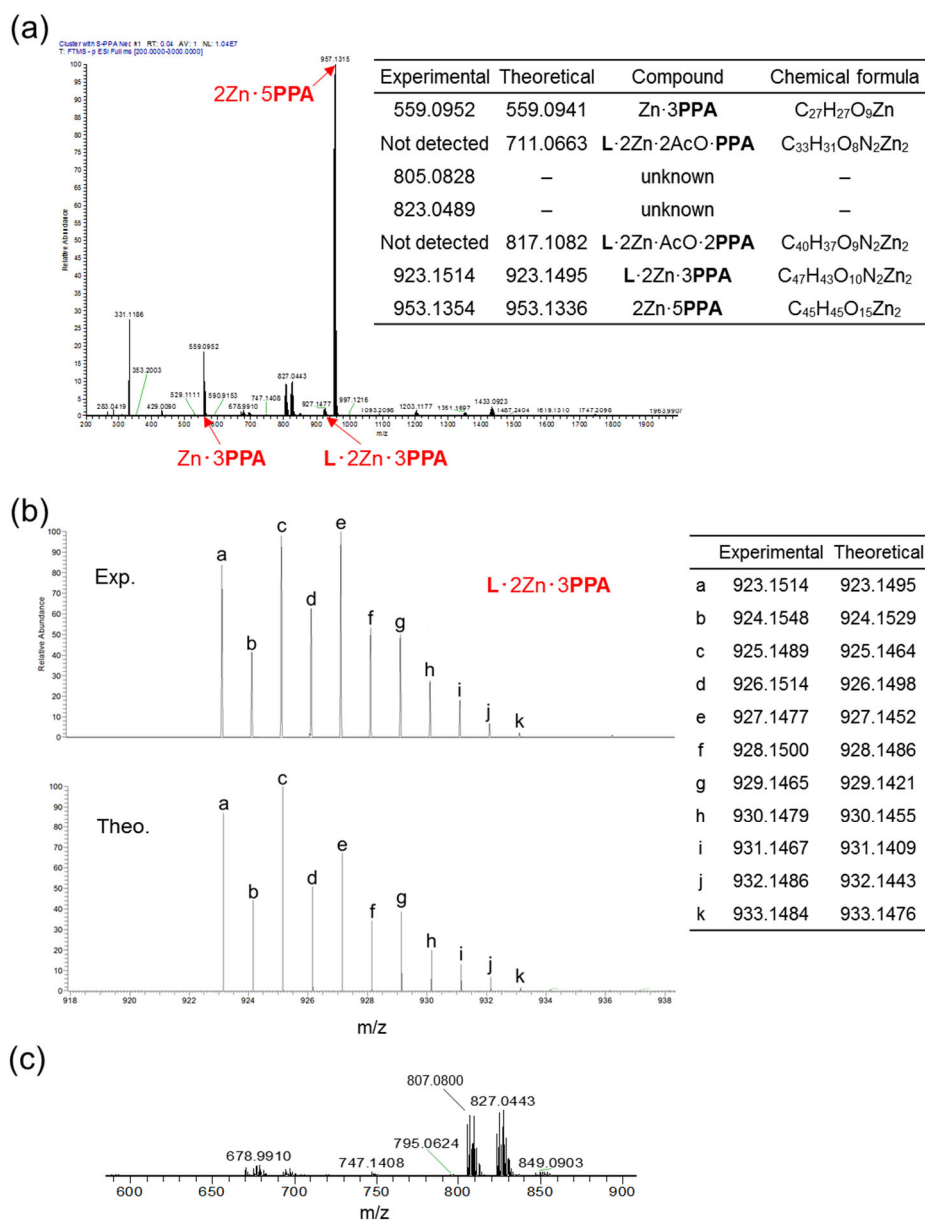849.0903
678.9910
747.1408

m/z

Figure S30. (a) ESI-MS spectrum of **L**·2Zn·3**PPA** in CDCl$_3$ (1 mM of **L**, 2 mM of zinc acetate, 8 mM (*S*)-**PPA**) in negative-ion detection mode. Signal due to **L**·2Zn·3AcO and **L**·Zn·AcO are absent, and that of **L**·2Zn·3**PPA** appears as a low intensity signal. Since 8 equiv. of **PPA** is sufficient to saturate the equilibrium of co-ligand exchange, partly exchanged species such as **L**·2Zn·2AcO·**PPA** and **L**·2Zn·AcO·2**PPA** could not be observed. Some of the more intense peaks could be assigned as clusters of Zn^{2+} and **PPA** (Zn·3**PPA**, 2Zn·5**PPA**). (c) ESI-MS spectrum expanded in the range 600−900 m/z, revealing that peaks due to **L**·2Zn·2AcO·**PPA** (711.0663 m/z) and **L**·2Zn·AcO·2**PPA** (817.1082 m/z) could not be observed.
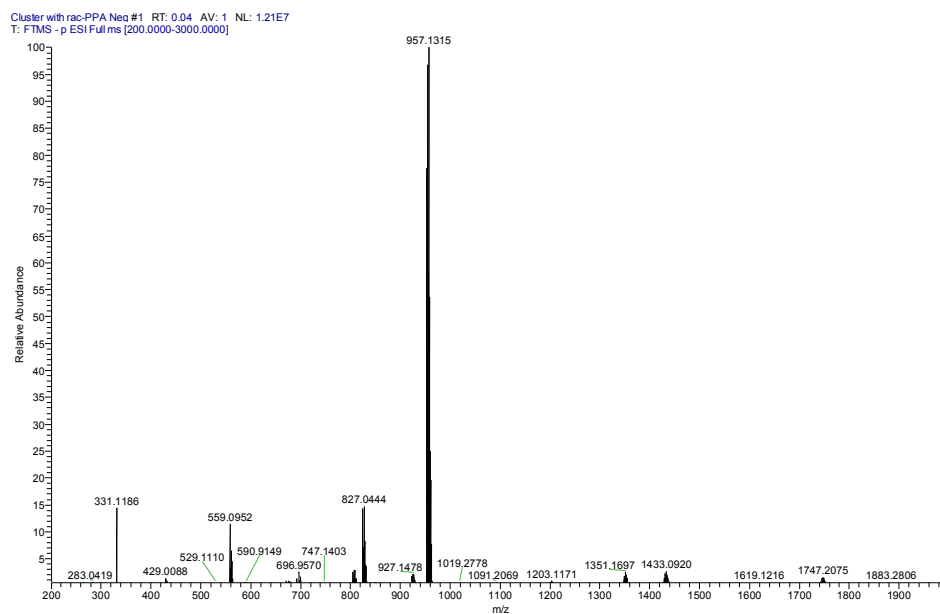
Figure S31. ESI-MS spectrum of **L**·2Zn·3**PPA** in CDCl₃ (1 mM of **L**, 2 mM of zinc acetate, 8 mM (*rac*)-**PPA**) in negative-ion detection mode.
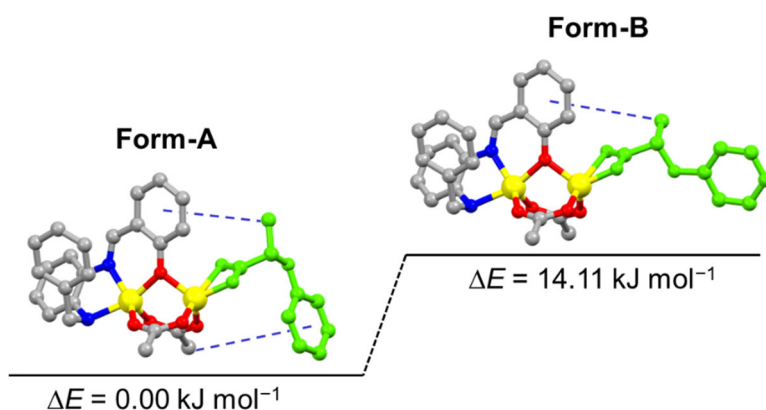
8. DFT calculation

Figure S32. The possible two conformations (form-A and form-B) of (*S*)-**PPA** in the ternary mixture were estimated at the X3LYP/3-21G(d) level ((*S*)-**PPA** is highlighted in green). Form-A, where two non-covalent interactions (denoted by blue lines) are involved, is more stable than Form-B with only one non-covalent interaction. Based on this stable conformation (i.e., Form-A), the other structures of ternary mixtures (Fig. 4) were calculated.
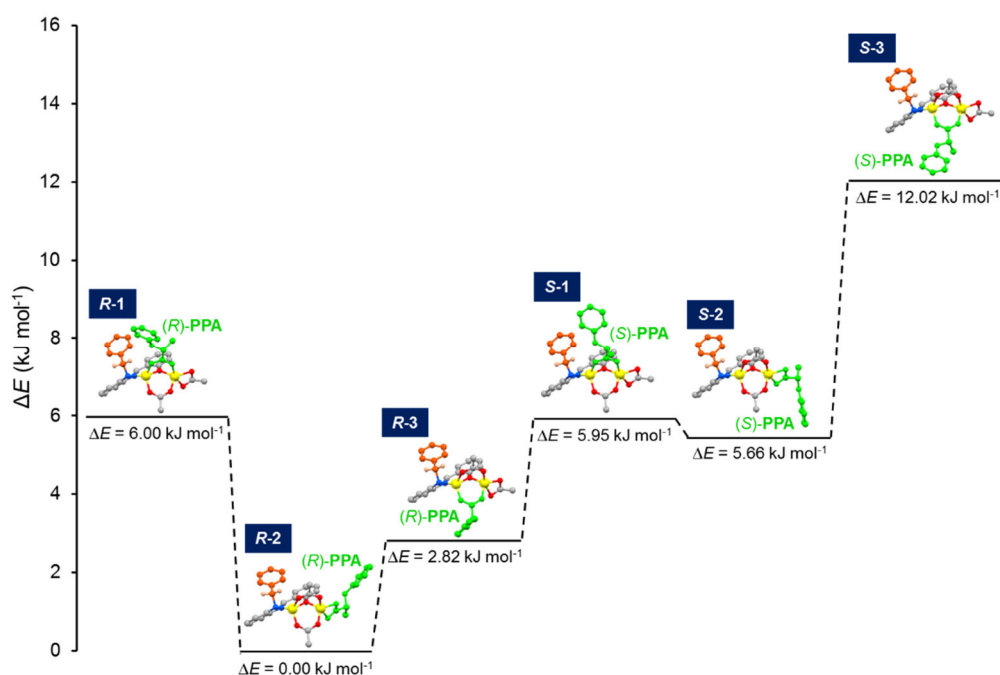

Figure S33. Energy diagram of the optimized structures of the zinc complex (**L·2Zn·3C**) with each of the three acetates substituted by **PPA** (in vacuum, 0 K) at X3LYP/6-31G(d) level. Benzyl group (with two CH_2 protons) and **PPA** are highlighted in orange and green, respectively.
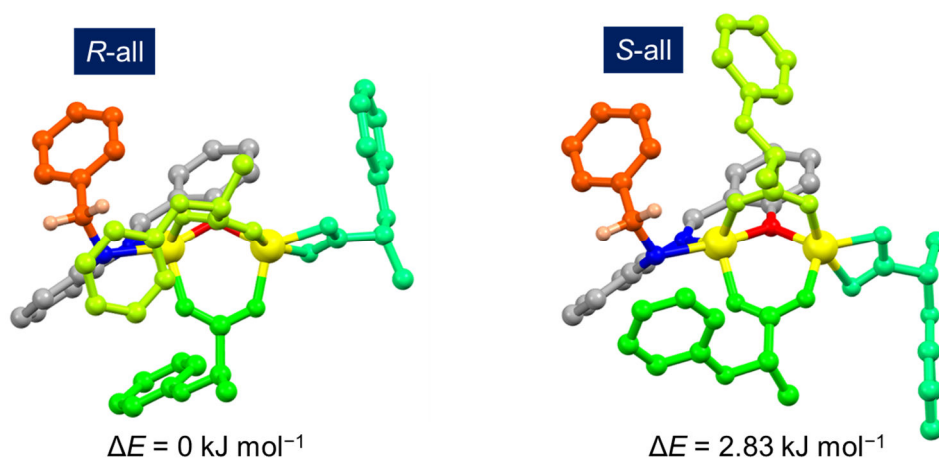
Figure S34. Optimized structures and their relative energy (Δ*E*) of **L·2Zn·3C** with all three acetates substituted by (*S*)-**PPA** or (*R*)-**PPA**, obtained at the X3LYP/6-31G(d) level (in vacuum, 0 K). Benzyl groups and **PPA** are highlighted in orange and green, respectively. Note that there are many possibilities of initial geometry in calculation, and initial geometry could largely influence the final optimized structure.
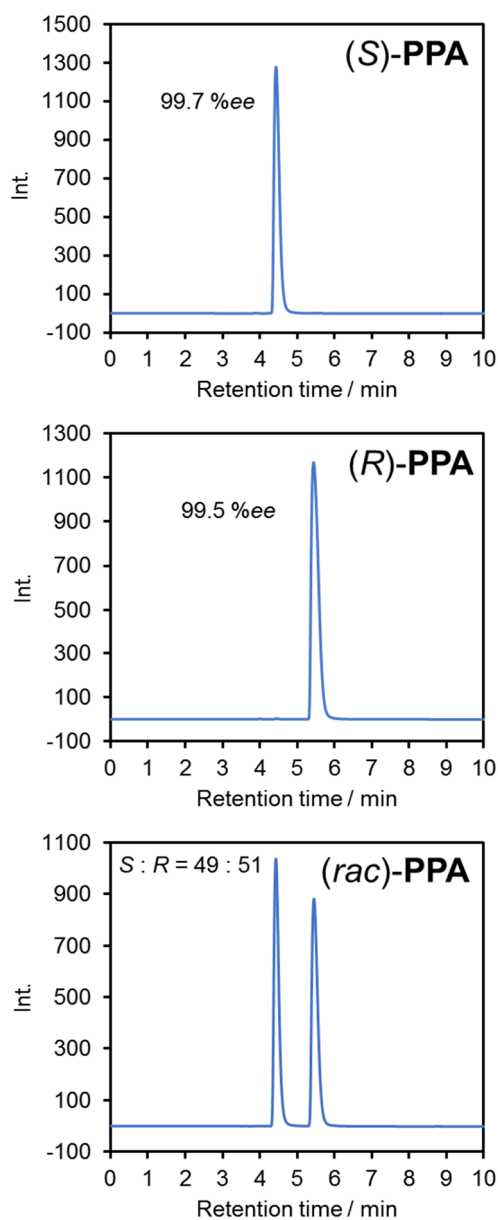
9. Chiral HPLC

Figure S35. Chiral HPLC chromatogram for **PPA** (CHIRALPAK IB, 4 mm (i.d.) × 25 cm, DAICEL, Japan) at a flow rate of 1.0 mL/min. Eluent was *n*-hexane/2-propanol/trifluoroacetic acid (87:13:0.5 v/v/v)[S11] with monitoring wavelength of 278 nm. *ee*% of **PPA** was estimated as being >99.5.

10. References

(S1) CrystalClear, Data collection and processing software, Rigaku Corporation, Japan, 2010.

(S2) CrysAlisPro, Data collection and processing software, Rigaku Corporation, Japan, 2015.

(S3) SHELXT 2018/2; Sheldrick, G. M. *Acta Crystallogr., Sect. A: Cryst. Phys., Diffr., Theor. Gen. Crystallogr*. **2014**, *70*, C1437.

(S4) CrystalStructure 4.3, Crystal structure analysis package, Rigaku Corporation, Japan, 2019.

(S5) SHELXL-2018/3: Sheldrick, G. M. *Acta Crystallogr., Sect. C: Cryst. Struct. Commun.* **2015**, *71*, 3.

(S6) PLATON: Spek, A. L. *Acta Crystallogr., Sect. D: Biol. Crystallogr.* **2009**, *65*, 148.

(S7) Frisch, M. J. et al. Gaussian 16, Revision B.01, Gaussian, Inc., Wallingford, CT, 2016.

(S8) Xu, X.; Goddard III, W. A. *Proc. Natl. Acad. Sci. U.S.A* **2004**, *101*, 2673.

(S9) Zimányi, L. *J. Phys. Chem. B*, **2004**, *108*, 4199.

(S10) Zimányi, L.; Kulcsár, Á.; Lanyi, J. K.; Sears, D. F.; Saltiel, J. *Proc. Natl. Acad. Sci. U.S.A* **1999**, *96*, 4408.

(S11) Ghanem, A.; El-Behairy, M. F.; Al-Ahdal, M. N. *Chromatographia* **2007**, *65*, 681.